ADVANCING EARTH AND SPACE SCIENCES

Earth and Space Science

RESEARCH ARTICLE
10.1029/2025EA004541

Aerial and Space-Borne Seismology on Venus: Viability and Design Implications for Future Missions

Quentin Brissaud[1], Chenxi Kong[2], Marouchka Froment[1], John Wilding[2], Anna J. P. Gülcher[3], Jennifer M. Jackson[2], Iris van Zelst[4], Raphaël F. Garcia[5], Celine Marie Solberg[6,7], and Sven Peter Näsholm[1,6]

[1]NORSAR, Kjeller, Norway, [2]Seismological Laboratory, California Institute of Technology, Pasadena, CA, USA, [3]Center for Space and Habitability, University of Bern, Bern, Switzerland, [4]School of GeoSciences, University of Edinburgh, Edinburgh, UK, [5]Institut Supérieur de l'Aéronautique et de l'Espace ISAE-SUPAERO, Université de Toulouse, Toulouse, France, [6]Department of Informatics, University of Oslo, Oslo, Norway, [7]Kongsberg Defence & Aerospace, Asker, Norway

Key Points:

- We built a probabilistic model to assess the detectability of venusquakes from Venus' atmosphere and space using physics-based simulations
- Detectability levels reach 65% at 1 s wave period for 6-month balloon-network or dayglow missions, but are below 10% for nightglow
- Seismic velocity/attenuation, noise, seismicity, mission duration, and airglow coupling efficiency are key aspects driving detectability

Supporting Information:

Supporting Information may be found in the online version of this article.

Correspondence to:

Q. Brissaud,
quentin@norsar.no

Citation:

Brissaud, Q., Kong, C., Froment, M., Wilding, J., Gülcher, A. J. P., Jackson, J. M., et al. (2026). Aerial and space-borne seismology on Venus: Viability and design implications for future missions. *Earth and Space Science*, *13*, e2025EA004541. https://doi.org/10.1029/2025EA004541

Received 2 JUL 2025
Accepted 7 MAY 2026

Author Contributions:

Conceptualization: Quentin Brissaud, Jennifer M. Jackson, Sven Peter Näsholm
Data curation: Quentin Brissaud, Chenxi Kong, Iris van Zelst, Celine Marie Solberg, Sven Peter Näsholm
Formal analysis: Quentin Brissaud, Chenxi Kong, Anna J. P. Gülcher, Jennifer M. Jackson
Funding acquisition: Quentin Brissaud, Sven Peter Näsholm
Investigation: Quentin Brissaud, Chenxi Kong, John Wilding, Anna J. P. Gülcher, Jennifer M. Jackson, Raphaël F. Garci
Methodology: Quentin Brissaud, Chenxi Kong, John Wilding, Anna J. P. Gülcher, Jennifer M. Jackson

Abstract Venus' evolution remains a mystery because of the lack of in situ geophysical data to constrain its interior structure. Recently-selected planetary missions VERITAS (NASA), DAVINCI+ (NASA), and EnVision (ESA) will investigate the planet's interior, surface, and atmospheric chemistry. However, none of these missions includes sensors capable of accurately probing Venus' crustal and mantle properties. Seismometer deployments are challenging on Venus due to high surface temperature and pressure. Acoustic balloon measurements and airglow observations—that monitor Venus' upper atmosphere glow caused by chemical and radiative processes—have been suggested as alternatives to surface deployments. However, it is critical to assess the potential of such missions under realistic conditions of geology, atmospheric states, network geometry, and seismicity using physics-based modeling. We employ a probabilistic framework to investigate detection probabilities as a function of Signal-to-Noise Ratio (SNR) for airglow and acoustic balloon missions using wave simulations, thermodynamically-consistent seismic velocity models, and realistic seismicity estimates. Our results demonstrate that the probability of detecting a single venusquake at SNR $>$ 1 over 6 months is around 65% across an entire 3-balloon network of about 5,000 km extent. Probabilities using dayglow imager data are below 60% and below 10% using nightglow data. Seismo-volcanic sequences enhance detectability but only if high seismic activity occurs at multiple volcanoes. Long-duration missions with both airglow and balloon-borne sensors could allow seismic wave measurements over a broad range of frequencies. Our results are highly dependent on seismic velocities, attenuation, seismicity, noise levels, mission duration, and airglow-coupling efficiency which should be the focus of future studies.

Plain Language Summary The interior of Venus remains a mystery because we lack seismic data. Such data were key to constrain the Moon's and Mars' subsurface. While upcoming missions will study Venus' surface and atmosphere, they will not carry instruments capable of detecting seismic waves from the ground. Because Venus' surface is extremely hot and under intense pressure, deploying traditional seismometers is challenging. As an alternative, scientists have proposed using high-altitude balloons and orbiting airglow cameras to detect pressure waves or light emissions in the atmosphere that may be triggered by venusquakes. In this study, we apply physics-based models and probabilistic methods to evaluate how well balloon and airglow observations would detect seismic events under realistic atmospheric and geological conditions. We show that a balloon network covering about 5,000 km could detect at least one venusquake with up to 65% chance over a 6-month mission. The detection rates are below 60% when using airglow observations from orbit. Our findings suggest that the success of future seismology missions will depend on the development of better models for the seismicity, atmospheric and airglow propagation, as well as noise levels.

1. Introduction

The evolution and present dynamics of Venus remain a mystery due to the lack of in situ geophysical data to constrain its atmosphere and interior structure. To address important scientific questions regarding Venus' past and present conditions and its habitability, NASA and ESA have selected three missions to investigate aspects of its deep interior, surface, and atmospheric chemistry (Widemann et al., 2023). However, the collection of seismic data, as performed on Mars by the InSight seismometer (Lognonné et al., 2023), is key to developing accurate models of the planet's interior. Unfortunately, the high pressure and temperature at the surface of Venus will most

Project administration: Quentin Brissaud
Resources: Quentin Brissaud
Software: Quentin Brissaud, Chenxi Kong
Supervision: Quentin Brissaud, Jennifer M. Jackson
Validation: Quentin Brissaud, Marouchka Froment
Visualization: Quentin Brissaud, Chenxi Kong
Writing – original draft: Quentin Brissaud, Chenxi Kong, John Wilding, Anna J. P. Gülcher
Writing – review & editing: Quentin Brissaud, Chenxi Kong, Marouchka Froment, John Wilding, Anna J. P. Gülcher, Jennifer M. Jackson, Iris van Zelst, Raphaël F. Garci, Celine Marie Solberg, Sven Peter Näsholm

likely prevent long-duration deployments of seismic instruments beyond a few months (Kremic et al., 2020). Recently, the seismo-acoustic community has proposed new methodologies, called balloon-based and airglow-based seismology, to alleviate the need for ground-based measurements (Krishnamoorthy et al., 2019). As seismic waves couple to the atmosphere, they excite low-frequency acoustic waves—infrasound—which propagate to high altitudes. These waves carry information about the source and the subsurface, enabling subsurface seismic imaging from high altitudes. Several detections of seismic waves in pressure waveforms recorded by stratospheric balloons have already been reported on Earth (Brissaud et al., 2021; Garcia et al., 2022), and a recent study showed that the source location and subsurface structure can be constrained using such data (Froment et al., 2025). Balloons carrying microbarometers flying in Venus' cloud layer between 45 and 60 km altitude, where pressure and temperature are similar to Earth's surface, could therefore detect the small pressure fluctuations induced by venusquake ground motion. At higher altitudes, above 90 km, acoustic waves can affect the transport of O_2 molecules on the night side of Venus, modulating the nightglow emission. Acoustic waves also cause adiabatic temperature variations, which can perturb energy transitions of CO_2 molecules, modulating the dayglow. These light emission perturbations can be sensed by satellites equipped with infrared-sensitive cameras (Garcia et al., 2024).

Assessing the feasibility of balloon-borne seismology in the Venus context is critical to the design of future mission concepts. In particular, the required mission duration to ensure the detection of significant seismic events is unclear. Interestingly, owing to Venus' dense atmosphere, the coupling between the ground and the atmosphere is significantly stronger than on Earth, which could enable detecting lower-magnitude venusquakes (Averbuch et al., 2023). Yet, the absence of global plate tectonics on Venus likely drastically reduces the occurrence of large-magnitude quakes (e.g., Van Zelst et al., 2024b). Recently, Garcia et al. (2024) provided a preliminary framework to address these research questions for mission scenarios using a ground-based seismic instrument, a single atmospheric balloon equipped with a microbarometer, or an airglow imager. Garcia et al. (2024) determined the minimum number of seismic events needed to obtain an arbitrary 66% detection probability, for at least one of these events, from each of the instruments. Garcia et al. (2024) concluded that seismic activity on Venus consisting of about 100 $m_w 5$ events over a 6-month balloon mission, or less than 10 events for an airglow mission, should be enough to ensure the detection of one seismic event.

There are several limiting assumptions in Garcia et al. (2024) that deserve further investigation: (a) The seismic activity was assumed to be homogeneous across the planet (as in Van Zelst et al., 2024b), despite the non-uniform spatial distribution of regions with more seismically-active potential, such as Venusian rifts, or dozens of "corona" structures– circular volcano-tectonics features defined by a (partial) ring of closely-spaced fractures– which have been proposed to be geologically active and have a non-random global distribution (Cascioli et al., 2025; Davaille et al., 2017; Gülcher et al., 2020); (b) Seismic amplitudes were modeled using an empirical relation between magnitude and peak seismic velocity designed for Earth scenarios. Thus, investigating the effect of seismic properties on detectability was not possible; (c) Only single-instrument and single-balloon detectability were estimated. Yet, to retrieve subsurface properties at various scales, airglow and/or acoustic balloon measurements of the same events should be performed, as acoustic-to-airglow coupling is less efficient at high frequencies (Kenda, 2018). Therefore, determining the probability of observing the same event across all instruments is critical for future missions; (d) Results were provided at 66% confidence level. Yet, mission designs should likely consider higher confidence levels to ensure the detection of seismic events; (e) The study used a binary condition to define detectability, which is that the signal level exceeds that of the noise, but details such as considering other Signal-to-Noise Ratios (SNRs) of detectable events were not considered. While this was a reasonable first step, the ability to detect signals at sufficiently high SNR is critical to properly distinguish different kind of seismic arrivals (surface waves, body waves and their multiples) and perform subsurface velocity inversions; (f) Finally, only seismic events of seismo-tectonic origin were considered, and seismo-volcanic events were not included in the analysis. Yet, recent volcanic activity on Venus has been detected in Magellan data (Herrick & Hensley, 2023; Sulcanese et al., 2024) and could constitute a major source of seismic waves.

In this contribution, we build a more comprehensive physics-based probabilistic framework to address these limitations, producing robust detectability estimates for seismic waves on Venus. Although Venus' seismicity remains mostly unknown, we apply and adapt two recently proposed seismicity models (Sabbeth et al., 2023; Van Zelst et al., 2024b) to account for the spatial heterogeneity in seismicity (Section 2.1). Instead of relying on empirical amplitude relations, we numerically model wave propagation and coupling for realistic seismic and atmospheric media (Section 2.2). Additionally, we produce detectability estimates for multi-instrument missions

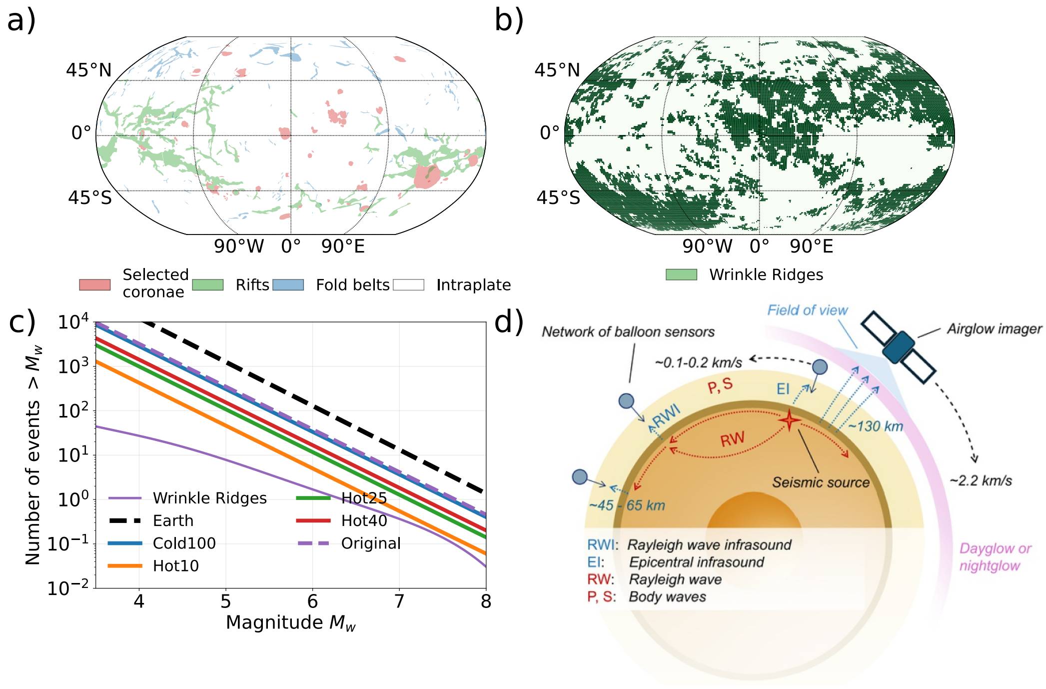

Figure 1. Seismicity and seismo-acoustic amplitude prediction models. (a) Tectonic settings on Venus as considered in Van Zelst et al. (2024b), derived from global geologic maps by Price and Suppe (1995); Price et al. (1996), adapted with a down-selection of coronae based on recent suggestions of plume-induced crustal recycling at certain coronae (Cascioli et al., 2025), (b) Global wrinkle ridge map from Bilotti and Suppe (1999) used in Sabbeth et al. (2023), (c) Seismicity estimates used in this study for each velocity model, wrinkle ridges (purple), and estimates from Van Zelst et al. (2024b) with Earth (dashed black) and the upper bound of low seismicity referred as Original (dashed purple), and (d) schematic of seismically generated infrasound (source location marked by the read star) and detection by microbarometers onboard balloons or from an airglow imager.

deploying balloon networks or airglow imagers (Section 2.3). Importantly, our probabilistic framework produces detection probabilities in terms of SNR, which facilitates sensitivity analysis at any noise level (Section 3). Finally, we investigate the detectability of Earth seismo-volcanic sequences, serving as a proxy for volcanism on Venus (Section 4).

2. Methods

Our main objective is to estimate the probability of detecting seismic waves in balloon pressure or airglow signals exceeding a given SNR, along a given balloon or airglow mager trajectory. This is based on a four-step procedure (see workflow in Section SI 1 in Supporting Information S1): (a) Based on magnitude-frequency distribution models, we compute the probability of venusquakes over a given magnitude, for each surface location, (b) We determine the pressure/airglow amplitude at each distance of venusquake-induced infrasound at the balloon altitude using numerical simulations, (c) We estimate the likelihood of observing a signal above a given SNR from a fixed location using steps (a) and (b), and (d) We integrate the detection likelihood estimates computed in step (3) along a given trajectory.

2.1. Venus Seismicity Estimates

The spatial and temporal distribution of venusquakes is based on Van Zelst et al. (2024b), with modifications accounting for predictions by Gülcher et al. (2025); Cascioli et al. (2025), and Sabbeth et al. (2023). Van Zelst et al. (2024b) assumed that Venus' tectonic settings are seismically analogous to specific terrestrial settings. Venus' tectonic settings were classified into four categories: fold belts, rifts, coronae, and intraplate regions. The spatial distribution of the first three is based on global maps by Price and Suppe (1995); Price et al. (1996), while the areas outside these tectonic regions are defined as intraplate (Figure 1a). Van Zelst et al. (2024b) assumed these Venus settings to be seismically analogous to Earth's continental collision zones (fold belt analog), continental rifts (rift analog), subduction zones (corona analog), and intraplate regions. With these Venusian tectonic regimes and Earth analogs, the number of venusquakes per year can then be estimated by scaling the number of seismic events in the corresponding terrestrial tectonic settings to Venus's dimensions. Scaling factors were built on the basis of the ratio between seismogenic thickness on Venus and Earth (Van Zelst et al., 2024b). That work considered three global seismicity scenarios: Inactive, Low Activity, and High Activity. In the Inactive scenario, the whole planet was assumed to have background seismicity analogous to Earth's continental intraplate setting. In the other two scenarios, ridges, rifts, and intraplate regions were considered seismically active, but in Low Activity, 27.8% of the total corona surface is active, whereas in High Activity, all coronae are active.

Because subduction zones are among Earth's most seismically active regions and produce the largest events, the assumption linking corona activity to terrestrial subduction strongly influences Van Zelst et al. (2024b)'s conclusions. Especially the High Activity scenario results in a number of quakes per year on the same order as on Earth. Coronae are prevalent on Venus, with 740 features recently cataloged (Gülcher et al., 2025). Their tectonic formation has been attributed to various lithospheric responses above either buoyant or transient mantle plumes (e.g., Dombard et al., 2007; Grindrod & Hoogenboom, 2006; Gülcher et al., 2020; Schools & Smrekar, 2024), or above gravitational instabilities and lithospheric downwellings (Hoogenboom & Houseman, 2006; Piskorz et al., 2014). Morphological evidence, analog experiments, and thermo-mechanical modeling suggest that short-lived retreating subduction can occur along coronae arcs (Cascioli et al., 2025; Davaille et al., 2017; Gülcher et al., 2020, 2023; Sandwell & Schubert, 1992). However, it is unlikely that all Venus' coronae are analogs to active terrestrial subduction zones. To produce more realistic detectability estimates, we consider only Van Zelst et al. (2024b)'s Inactive and Low Activity scenarios. Furthermore, we refine the global distribution of coronae that are considered seismically active based on a recent study of their topographic and gravity signatures (Cascioli et al., 2025), which proposes active plume-induced crustal recycling scenarios (subduction or lithospheric delamination) to occur on 34 coronae today (Figure 1a, red features). This refinement enables more meaningful spatially-dependent detectability estimates for these features. For simplicity, we keep the subduction analog for these shortlisted coronae (Figure 1a). The scaling of the Venus seismic moment rate by Van Zelst et al. (2024b) was based on a 8–23 km seismogenic thickness. Here, we follow Maia et al. (2024), assuming the seismogenic thickness to match the 600°C isotherm. Hence, we derive the seismogenic thickness based on each geotherm profile of the geological model (Appendix A).

Sabbeth et al. (2023), estimated the total seismic moment release based on mapped wrinkle ridges, which are compressive anticlines at the surface caused by blind thrust faults at depth (Figure 1b). They determined the total fault length from the global wrinkle ridge map of Bilotti and Suppe (1999). By assuming an average vertical slip extent, three tiers of segmentation, and a given deformation duration, Sabbeth et al. (2023) estimated the annual seismicity for these mapped wrinkle ridges. These estimates remain conservative for two reasons. First, the wrinkle ridge map by Bilotti and Suppe (1999) captures global trends and overlooks many faults, thereby underestimating the total length of all wrinkle ridges (Bethell et al., 2019). Second, Sabbeth et al. (2023) considered a 100M year deformation time and only three tiers of segmentation, producing a seismicity rate multiple orders of magnitude below Earth. This results in detection probabilities close to zero for a short mission duration at high noise levels. To produce more optimistic, yet realistic estimates, we introduced two modifications to Sabbeth et al. (2023)' work by considering a 1M year deformation time and five tiers of segmentation. The resulting seismicity remains low, within the same order of magnitude as the inactive (intraplate) scenario of Van Zelst et al. (2024b), but orders of magnitude below estimates from tectonic feature scaling (Figure 1c).

2.2. Seismo-Acoustic Modeling

Body and Rayleigh waves excited by venusquakes can couple to the atmosphere as Epicentral infrasound and Rayleigh-wave infrasound, which can propagate to high altitudes (Figure 1d). We model venusquake-induced infrasound in a given frequency range using an ensemble of seismic models, source location, and focal mechanisms through a three-step procedure: (a) We compute seismic Green's functions to determine ground vertical velocity at global scale using the QSSP method implemented in the `Pyrocko` Python package (Heimann et al., 2019; Wang et al., 2017); (b) We convert ground vertical velocities to ground pressure using a plane-wave assumption; and (c) For balloon sensors, we scale the ground pressure, accounting for the balloon altitude. For the airglow, we scale the ground velocity to nightglow and dayglow photon emissions. Resulting waveforms can be bandpass filtered in a specific range to extract the peak amplitude versus distance from the epicenter. The seismic

10.1029/2025EA004541

modeling in (a) allows us to predict the peak amplitude for any 1-D layered seismic model and any point moment tensor source, while accounting for Venus' sphericity, which is important at global scales.

We build 1-D subsurface velocity models based on thermodynamic modeling and assuming three scenarios for the thermal profile and compositional changes with depth (details in Appendix A: and SI 2). Our three scenarios represent plausible lithological end-members (e.g., basaltic crust and granitoid crust) for cold and hot geotherms inspired by the interior thermal structures of Venus in Dumoulin et al. (2017). This model, built with a cold geotherm and 50 km granitoid crust, leads to a clear crust-mantle boundary, similar to the Preliminary Reference Earth Model (PREM). However, the two other basalt-harzburgite hot models exhibit a thick low-velocity zone which creates large shadow zones that reduce the peak velocity amplitudes. By using 1-D layered models, we ignore mode- and wave-conversion in regions of rapid lateral seismic velocity variations (Brissaud et al., 2020) and topographic scattering (Brissaud et al., 2021). Such path effects could occur on Venus in regions of rapid change in crustal thickness, compositional change, and topography (e.g., James et al., 2013). However, the best available crustal thickness models still only resolve smooth variations with dominant wavelength above 100 km, a scale too large to generate significant mode conversion.

The focal mechanism and focal depth are important parameters that control the far-field amplitude. To account for these source- and path-effects and their uncertainties, we simulate Green's functions for all combinations of velocity models, at 20 different focal depths up to 25 km depth, and for strike-slip and dip-slip mechanisms. Our 25 km focal depth bound corresponds to the upper estimates of the seismogenic thickness on Venus for the Cold100 model. Because we assume the seismogenic thickness is given by the 600°C isotherm (Maia et al., 2024), we set different maximum venusquake depths z_{geo} for each geological model. Strike-slip and reverse-faulting events correspond to end-members for peak vertical surface velocity, with strike-slip producing primarily horizontal motion and reverse, or normal, faults producing vertical motion. We then estimate the amplitude uncertainty by fitting a lognormal distribution, using a Maximum Likelihood Estimation implemented using the `scipy` library, to the peak amplitude realizations across all source- and velocity-model combinations. The amplitudes are not only focal mechanism dependent, but also frequency dependent, impacting the source time function and giving path effects. Source time functions are intimately related to rupture processes, which are hard to define empirically. We therefore consider a Dirac source time function to avoid making additional assumptions about the source physics. To facilitate the detectability analysis across the full spectrum, we discretize the frequency into three logarithmically distributed bands such that at 100 s: (0, 0.05) Hz, at 10 s: (0.05, 0.22) Hz, and at 1 s: (0.22, 1) Hz.

We use a straightforward scaling to convert seismic amplitude v_z (m/s) into ground pressure p_s (Pa) in step (2), given by $p_s = \rho_s c_s v_z$, where c_s (m/s) is the surface acoustic velocity, and ρ_s (kg/m^3) is the surface atmospheric density. In step (3), we scale the ground pressure amplitude to obtain the amplitude p_b at the balloon altitude using

$$p_b = \sqrt{\frac{\rho_b c_b}{\rho_s c_s}} p_s, \tag{1}$$

where ρ_b (kg/m^3) is the atmospheric density and c_b (m/s) the acoustic velocity, both defined at the balloon altitude. Horizontal wind data are extracted on 15 June 2025, from the Venus Climate Database (VCD, Lebonnois et al., 2010, 2016, 2022; Martinez et al., 2023). We use a single density profile extracted at the equator and longitude 0 (SI 2). This scaling assumes a vertically propagating plane wave in a layered atmosphere, that is, without considering geometrical spreading, refractions or reflections, which is a good approximation when dealing with Rayleigh waves (Gerier et al., 2024; Macpherson et al., 2023). As seismic velocities are much larger than acoustic velocities, surface waves excite large areas of the ground in a short amount of time, resulting mostly in vertically-propagating acoustic waves. This process is similar to plane waves emitted by fast-traveling meteors in the atmosphere. Using this approach, body wave amplitudes in pressure records near the epicenter can be overestimated due to the absence of geometrical spreading in our computation. However, epicentral waves are not expected to contribute significantly to detection probabilities as their amplitude decays much faster with distance than surface waves. The impact of horizontal winds on acoustic amplitudes is assumed to be insignificant for this nearly-vertical infrasound propagation. Attenuation is typically low below 1 Hz on Venus (Garcia et al., 2024). However, we consider attenuation in the airglow computations at higher altitudes (see Appendix D). Finally, the noise level σ_n is still unconstrained for Venus conditions. We assume σ_n to be frequency-independent and at the

10.1029/2025EA004541

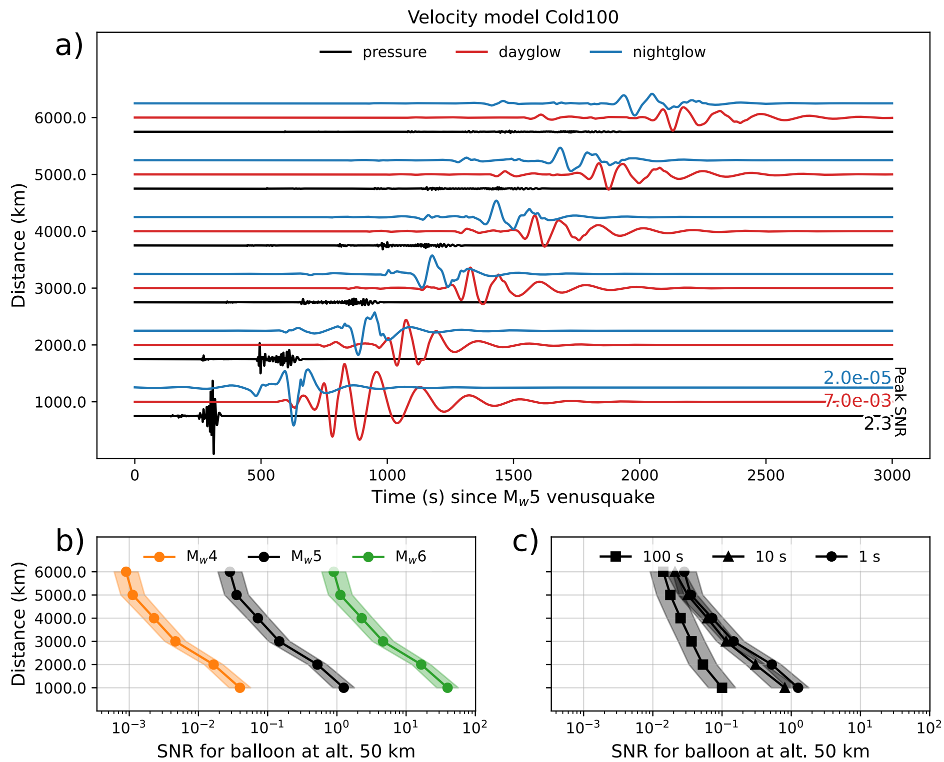

Figure 2. Seismo-acoustic amplitude based on the Cold100 velocity model. (a) Simulated SNR timeseries, high-pass filtered with the corner frequency 0.005 Hz for a M_w5 dip-slip venusquake (strike $\phi = 45°$, dip $\delta = 45°$, and rake $\lambda = 45°$) produced by a 5 s triangle source time function v. Northward distance from the source, for balloon pressure measurements at 60 km altitude (black), dayglow measurements (red), and nightglow (blue). (b) Median amplitude model at 1 s for a m_w4 venusquake (orange), m_w5 (black), and m_w6 (green) v. Distance, for a variety of focal mechanisms, source depths, and strikes, along with the 0.25 and 0.75 quantiles (shaded). (c) Median amplitude model for a m_w5 venusquake at period 100 s (square), 10 s (triangle), and 1 s (circle) v. Distance, for a variety of focal mechanisms, source depths, and strikes, along with the 0.25 and 0.75 quantiles (shaded).

same order of magnitude as balloon noise recorded on Earth, which is $\sim 10^{-2}$ Pa (Garcia et al., 2024). For airglow data, we consider shot noise to be the dominant source of noise and is given by $\sigma_{\text{shot noise}} \approx \sqrt{P}$, where P is the number of photons (Kenda, 2018, Section 4.4).

The resulting pressure timeseries are dominated by surface waves at teleseismic distances (Figure 2a, black line). In contrast to pressure signals, dayglow and nightglow conversions lead to strong attenuation at high frequency (Figure 2a, red and blue lines). Note that the volume emission rates peak at lower altitude for nightglow compared to dayglow, leading to earlier apparent arrival times in the nightglow. The balloon SNR decreases with source distance, but the median SNR remains above 1 up to 3,000 km range for a m_w5 venusquake (Figure 2b). We observe similar amplitudes at 1 and 10 s due to the presence of a strong crustal waveguide in the Cold100 model, leading to amplification of surface waves below 10 s, while longer periods consistently show lower amplitudes (Figure 2c). In contrast to Cold100, models built from hot geotherms that exhibit shadow zones lead to much lower SNR (SI 3). Note that the higher amplitude at short periods can also be explained by the use of a Dirac source time function to model venusquakes which is not a realistic representation of time-dependent rupturing behaviors observed in the far-field (Aki, 1972). Energy spectra of seismic waves in the far-field can be described using the notion of corner frequency, beyond which energy steeply decreases, capturing the impact of fault length and rupture velocity (Brune, 1970). Empirical relationships between source properties and corner frequency typically lead to much lower amplitude at high frequencies and therefore lower detection probabilities (SI 4). However, to avoid introducing a new set of parameters to capture the spectral decay of energy with frequency, we present results for a Dirac source in the remainder of this paper.

2.3. Venusquake Detection Probability Framework

Determining venusquake detection probabilities bears similarities with seismic hazard estimation, where the objective is to compute the probability that at least one earthquake generates ground motion exceeding a certain threshold (Cornell, 1968). Similarly, we want to determine the probability that at least one venusquake generates infrasound signals exceeding a certain SNR. This can therefore be described as a Poisson process assuming that the distribution of events over a given period of time follows a Poisson distribution in each tectonic region. We can then determine this detection probability as

$$\mathbb{P}\left(\mathrm{SNR} > d, M_{\mathrm{w,min}}, x^{\mathrm{obs}}_{\mathrm{lat,lon}}, t\right) = 1 - \exp[-\lambda(\mathrm{SNR} > d)t], \tag{2}$$

where $\mathbb{P}\left(\mathrm{SNR} > d, M_{\mathrm{w,min}}, x^{\mathrm{obs}}_{\mathrm{lat,lon}}, t\right)$ is the probability of observing at least one event at $\mathrm{SNR} > d$ from a balloon location $x^{\mathrm{obs}}_{\mathrm{lat,lon}}$, for events with $M_{\mathrm{w}} \geq M_{\mathrm{w,min}}$, at a balloon noise level σ_n (Pa), and a mission duration t (years). We denote by $\lambda(\mathrm{SNR} > d)$ the rate of venusquakes producing an SNR exceeding d. In the rest of the manuscript, we refer to the probability of observing at least one event with SNR exceeding d as the probability of detecting venusquakes. The rate λ depends on the yearly rate of venusquakes above a magnitude $M_{\mathrm{w,min}}$ in each tectonic region, expressed as $\lambda^{\mathrm{tec}}(M_{\mathrm{w}} > M_{\mathrm{w,min}})$, as well as on the probability of detecting venusquakes from that region from the balloon location $\mathbb{P}(\mathrm{SNR} > d|\mathrm{tec})$, such that

$$\lambda(\mathrm{SNR} > d) = \sum_{\mathrm{tec}} \lambda^{\mathrm{tec}}(M_{\mathrm{w}} > M_{\mathrm{w,min}})\mathbb{P}(\mathrm{SNR} > d|\mathrm{tec}). \tag{3}$$

The yearly rate of venusquakes is provided by the seismicity estimates for a given seismicity scenario (Section 2.1). As for the probability of detecting venusquakes from a given tectonic region $\mathbb{P}(\mathrm{SNR} > d|\mathrm{tec})$, it is obtained by integrating the probability of detecting a specific event over the range of possible magnitudes and source distances, which reads

$$\mathbb{P}(\mathrm{SNR} > d|\mathrm{tec}) = \int_{M_{\mathrm{w}}=M_{\mathrm{w,min}}}^{M_{\max}} \int_{r=0}^{r_{\mathrm{Venus}}} \mathbb{P}(\mathrm{SNR} > d|M_{\mathrm{w}}, r) f_M^{\mathrm{tec}}(M_{\mathrm{w}}) f_R^{\mathrm{tec}}(r)\, dr\, dM_{\mathrm{w}}, \tag{4}$$

where $\mathbb{P}(\mathrm{SNR} > d|M_{\mathrm{w}}, r)$ is the probability of detecting venusquakes of a given magnitude M_{w} from a distance r (km), r_{Venus} is the antipodal distance on Venus, that is, maximum distance between two locations, $f_M^{\mathrm{tec}}(M_{\mathrm{w}})$ is the Probability Density Function (PDF) of an event with a specific magnitude M_{w} occurring in the tectonic region tec, and $f_R^{\mathrm{tec}}(r)$ is the PDF of an event occurring in the tectonic region tec at a distance r from the sensor. These two PDFs read

$$f_R^{\mathrm{tec}}(r, \mathbf{x}) = \frac{\partial}{\partial r}\mathbb{P}(R < r) = \frac{\partial}{\partial r}\frac{\mathcal{S}(r, \mathbf{x}) \cap \mathcal{S}_{\mathrm{tec}}}{\mathcal{S}_{\mathrm{tec}}}, \tag{5}$$

$$\mathcal{S}(r, \mathbf{x}) = \{P \in \mathrm{Venus} : \mathrm{dist}(P, \mathbf{x}) \leq r\}, \tag{6}$$

$$f_M^{\mathrm{tec}}(M_{\mathrm{w}}) = \frac{\partial}{\partial M_{\mathrm{w}}}\mathbb{P}(M_{\mathrm{w}} \geq M \geq M_{\mathrm{w,min}}) = -\frac{\partial}{\partial M_{\mathrm{w}}}\frac{\lambda^{\mathrm{tec}}(M_{\mathrm{w}} \geq M \geq M_{\mathrm{w,min}})}{\lambda^{\mathrm{tec}}(M \geq M_{\mathrm{w,min}})}, \tag{7}$$

where $\mathcal{S}_{\mathrm{tec}}$ is the surface area of tectonic region tec and $\mathcal{S}(r, \mathbf{x})$ is the projected circular surface area from balloon location $\mathbf{x}$ up to a distance r. Finally, the probability of detecting a specific venusquake $\mathbb{P}(\mathrm{SNR} > d|M_{\mathrm{w}}, r)$ used in Equation 4 corresponds to the probability of a venusquake to produce a signal with $\mathrm{SNR} > d$, integrated over all possible SNR values above d such that

$$\mathbb{P}(\mathrm{SNR} > d|M_{\mathrm{w}}, r) = \int_{\mathrm{SNR}=d}^{\infty} f_{\mathcal{A}}(\mathrm{SNR}; M_{\mathrm{w}}, r)\, d\mathrm{SNR}, \tag{8}$$

where $f_{\mathcal{A}}(\mathrm{SNR} = d; M_{\mathrm{w}}, r)$ is the PDF for the amplitude distribution $\mathcal{A}$ and for a specific venusquake to generate a signal with $\mathrm{SNR} = d$, which can be described by a lognormal distribution such that

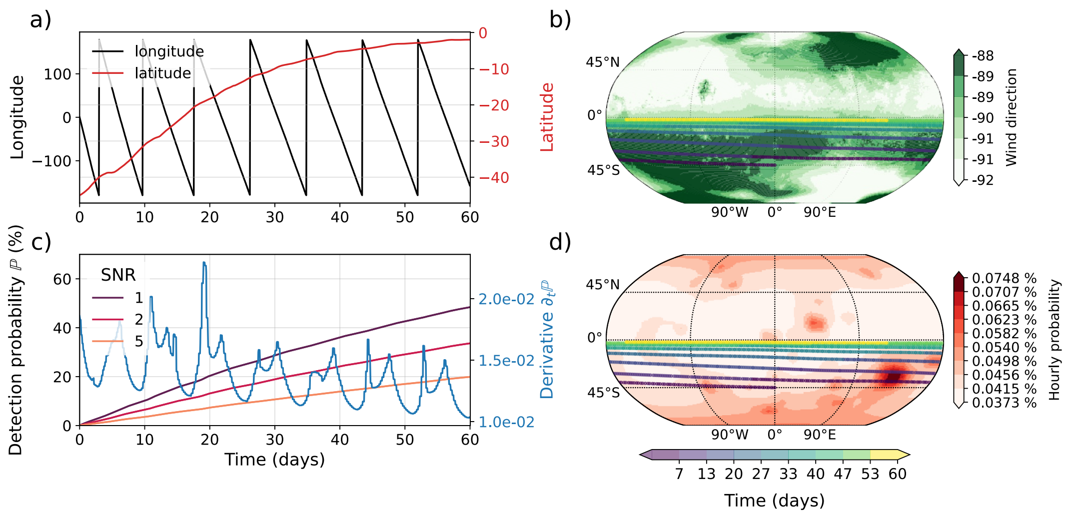

Figure 3. Tectonic event detection probability for a 2-month balloon flight at 50 km altitude, analyzed at period 1 s for Cold100 velocity model. (a) Balloon trajectories in longitude (black) and latitude (red). (b) Wind direction at 50 km altitude. The points show the trajectory, color-coded by time. (c) Detection probability SNR $= 1, 2, 5$ versus time (orange, red, purple lines) and time-derivative of the detection probability for SNR $= 1$ (blue line). (d) Hourly detection probability for SNR $= 1$. The points show the trajectory. The maps are in Robinson projection, centered at 0° longitude.

$$\mathcal{A} \sim \ln\mathcal{N}\left(\frac{\mathrm{TL}(M_\mathrm{w}, r)}{\sigma_n}, s_{\mathrm{TL}}(r)\right), \tag{9}$$

where $\ln\mathcal{N}$ is the lognormal distribution of scale $\mathrm{TL}(M_\mathrm{w}, r)/\sigma_n$ and shape $s_{\mathrm{TL}}(r)$. $\mathrm{TL}(M_\mathrm{w}, r)$, in Pa, stands for transmission loss, that is, the relative amplitude decrease with distance, and $\mathrm{TL}(M_w, r)$, in Pa, is the maximum synthetic amplitude prediction for an event of magnitude M_w at a distance r from the source, and the shape $s_{\mathrm{TL}}(r)$ captures the predicted uncertainties, also called theory error. Both scales and shapes are determined through a lognormal fit at each distance from the source of peak synthetic amplitudes for a range of focal depths and crustal thicknesses (Section 2.2). Note that the impact of larger noise levels can be investigated by simply looking at a higher target SNR in the results shown here.

Several additional aspects need to be included to reflect the complexity and multi-instrument capabilities of future geophysical missions. Firstly, balloons will move along Venusian winds. To include this effect, we simulate a trajectory from an initial drop-off location, considering a free-floating balloon moving with horizontal winds at constant altitude. Detection probabilities computed at each location can then be integrated along the balloon trajectory to determine the final detection probability at mission end (see Appendix Appendix B). Additionally, successful subsurface inversion requires accurate localization of seismic events, which can be achieved by combining observations from multiple locations (Froment et al., 2025). Therefore, assessing the detection of the same event across a balloon network is key. The balloon network detectability is estimated by varying the surface area $\mathcal{S}(r, \mathbf{x})$ in Equation 7 and considering the source-balloon distances as the maximum distance between sources across all balloons in the network (see Appendix Appendix C). Finally, airglow imagers can provide complementary acoustic wave observations, especially for large-magnitude events (Garcia et al., 2024). We incorporate airglow-based SNR estimates into the detectability framework by including the airglow imager detection surface in the surface area $\mathcal{S}(r, \mathbf{x})$, to account for both the expected SNR in airglow data and the large field-of-view of airglow imagers (see Appendix D).

3. Tectonic Event Detectability

To illustrate both our trajectory and detection probability estimates, we first consider the detectability of events produced by the tectonic seismicity model, built from Earth catalog scaling, from a single balloon being dropped off at an arbitrary location (0°E, 45°S). Trajectories for balloons flying at 50 km altitude are mostly westward (Figures 3a and 3b) due to the strong westward winds in Venus' upper atmosphere. Interestingly, a small meridional wind component (SI 2) causes the balloon to drift from high latitudes toward the equator. At higher altitudes, the meridional wind reverses, and balloons dropped off a few degrees off the equator slowly drift toward the poles (SI 5). Balloons can thus get trapped in polar regions if dropped off within 5° latitude from the poles. Figure 3c shows detection probabilities that steadily increase with flight time to reach about 45% for SNR $= 1$ after 2 months. We observe peaks in the time derivative of the detection probability (Figure 3c, blue line) corresponding to a sudden increase in detection likelihood as the balloon flies above the most active coronae (Figures 3a and 3d).

When considering long-duration flights, spatial heterogeneities in seismic activity (Figure 1c) do not significantly affect the final detection probability compared to a homogeneous global seismicity regardless of the drop-off location (SI 5). We obtain similar results at a period of 10 s, but the final detection probability drops at a period of 100 s due to lower amplitudes at low frequencies (SI 6). The presence of a strong crustal waveguide seems key to producing strong ground motions and detectable signals (SI 3), as velocity models built from hotter thermal profiles lead to lower final detection probabilities (SI 7). Beyond tectonic seismicity, the lower moment rates for wrinkle ridges lead to significantly lower detection probabilities, at less than 10%, after a 2-month mission at 1 s (SI 8). Results are presented for detection of at least one event, but the detection of several events could ensure more robustness in inverted subsurface and source models. Hourly detection probabilities would drastically decrease for the detection of at least two events or more when integrated along a balloon path (SI 9).

Robust probability estimates should not be dependent on a specific balloon trajectory since drop-off locations are not constrained yet. We therefore simulated 6-month flights at four altitudes (50, 55, 60, and 65 km), and from 750 different drop-off locations (latitude 65°S to 65°N, excluding the poles). Median probabilities and quantiles 0.25 and 0.75 were extracted from this simulation set. Statistics are computed for: (a) a single balloon, (b) a 3-balloon network dropped-off along the same latitude line with a maximum distance of 5,000 km, and (c) a nightglow or dayglow imager. Due to the peak ground velocity increase with frequency, we observe a significantly higher final detectability level after 6 months (Figures 4a–4c) at 1 and 10 s ($>75\%$ for a single balloon) than at 100 s ($\sim 50\%$ for a single balloon). We also observe up to 10% variability in detectability between the 0.25 and 0.75 quantiles, mainly due to different balloon flight altitudes and decreasing pressure with altitude. At 1 s, detection probabilities of the same event across the entire network show a 30% decrease compared to a single-balloon detection across a balloon network (Figure 4c). The variability in detectability between network configurations decreases below $\sim 15\%$ for lower frequencies (Figures 4a and 4b). This is likely due to the increased attenuation of high-frequency seismic motion, preventing its propagation at global scales. Detection probabilities decrease by about $25-35\%$ between SNR $= 1$ and SNR $= 5$ for all periods (Figures 4d–4f). High SNR is generally reached for high-magnitude events, which produce high-amplitude surface waves that travel globally. On the other hand, detecting any event from a network slightly increases the detection probability for low SNR thresholds. At 100 s, where predicted amplitudes are lower, both network- and single-balloon detection probabilities converge to lower values due to the absence of detectable signals at a global scale.

Detection probabilities are also highly dependent on the seismic velocity model, as suggested by hourly detection probability maps (SI 7). Detectability levels for a 3-balloon network decrease by at least 40% when using models built from hot geotherms (Figures 4g–4i). The presence of a strong crust-mantle interface in Cold100 explains the larger final probabilities. Model Hot40, despite not exhibiting a large low-velocity zone in the upper mantle, still produces detection probabilities on the same order as the other models built from hot geotherms. Airglow imagers typically yield a much lower detection probability than balloon networks: at most 60% above 10 s in the dayglow layer even when considering the binning of 7×7 pixels over 10 s (Figures 4j–4l). Binning $N \times N$ pixels or N^2 time steps increases the SNR by a factor N but also decreases the spatial or time resolution of each observation (Kenda, 2018). With the predicted airglow SNR being 3 orders of magnitude lower than balloon detections, airglow detections show small detection probabilities after 6 months (below 60% in the dayglow and below 10% in the nightglow) despite benefiting from a large field of view (FOV). In contrast to balloon detectability, the low-pass filtering effects from integration of volume emission rate perturbations in the airglow layer lead to significant attenuation at 1 s. Comparing Figures 4d–4f and 4j–4l, for low-SNR signals, the detectability of a single seismic event across both balloon and airglow sensors will therefore be mostly restricted by airglow detectability.

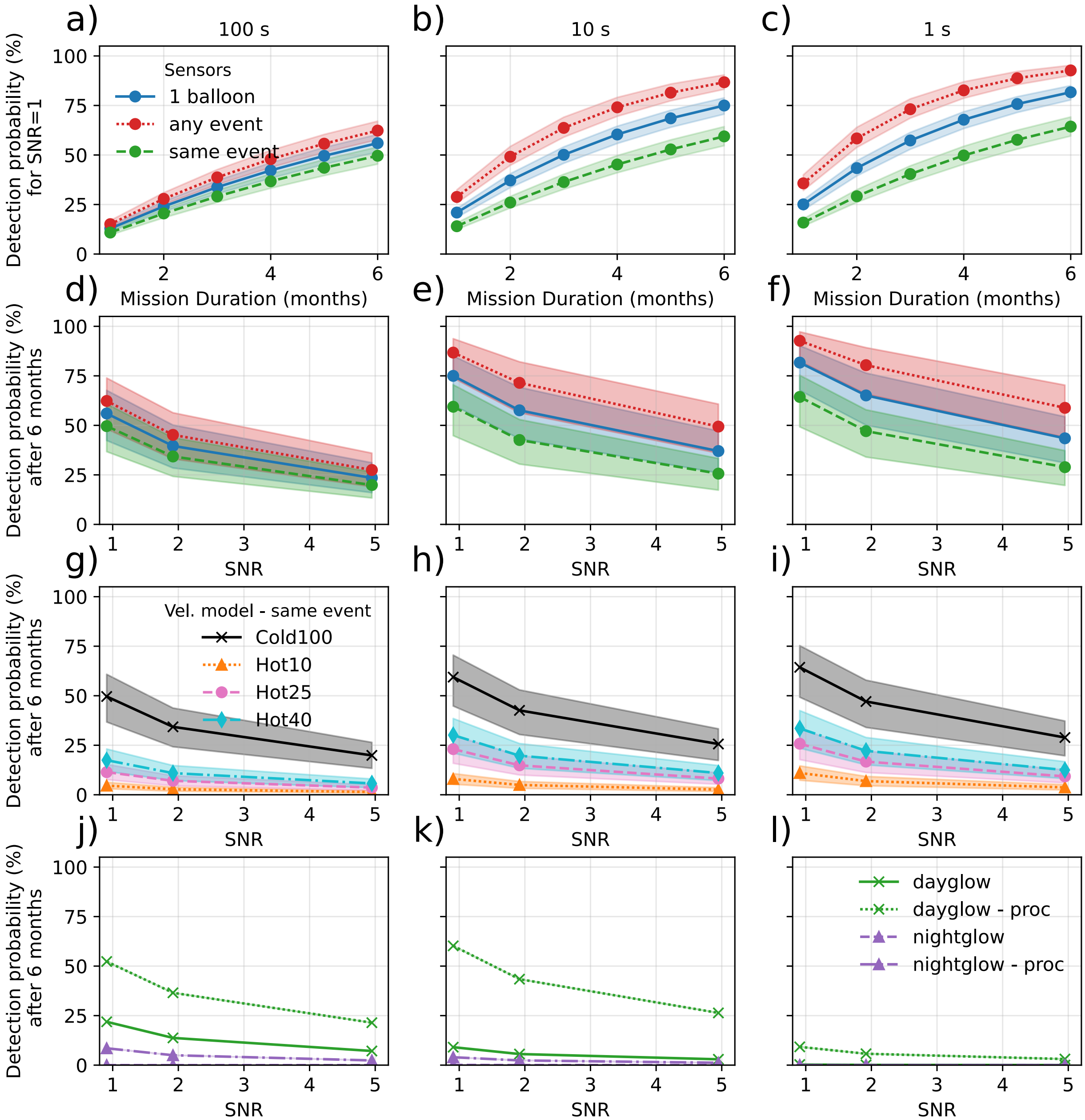

Figure 4. Tectonic event detection probability for balloon and airglow networks. Median detection probabilities (solid lines) and uncertainty (shaded), computed from the quantiles 0.25 to 0.75, for wave periods (a, d, g) 100 s (b, e, h) 10 s, and (c, f, i) 1 s. For the Cold100 velocity model (a, b, c) Detection probability v. Mission duration for SNR $= 1$ and (d, e, f) Detection probability v. SNR over a 6-month mission for a single balloon (1 balloon, blue circle) and for a 3-balloon network (any event and same event) averaged over all drop-off locations. The estimated balloon network detection probabilities are shown for the detection of a single event at all balloons across the network (same event, green circle) and for the detection of any event by at least one balloon in the network (any event, red circle). (g, h, i) Detection probability v. SNR over a 6-month mission for a balloon network under the Cold100 velocity model (black), Hot10 (orange), Hot25 (pink), and Hot40 (blue) (j, k, l) Detection probability v. SNR over a 6-month mission for velocity model Cold100 for an airglow imager probing the dayglow (green cross), nightglow (purple triangle) with postprocessing (7×7 pixel binning and 10-s time binning, dashed lines) and without postprocessing (solid lines).

4. Volcanic Sequence Detectability

In addition to major tectonic structures, Venus' surface is largely dominated by volcanic features (e.g., Ghail et al., 2024), with at least tens of thousands of volcanoes, flows, and edifices identified (Bickel et al., 2025; Hahn & Byrne, 2023). Given that major terrestrial volcanoes are seismically active (Phillipson et al., 2013), similar activity may also occur on Venus. The detection of volcanic seismicity would bring a better understanding of the

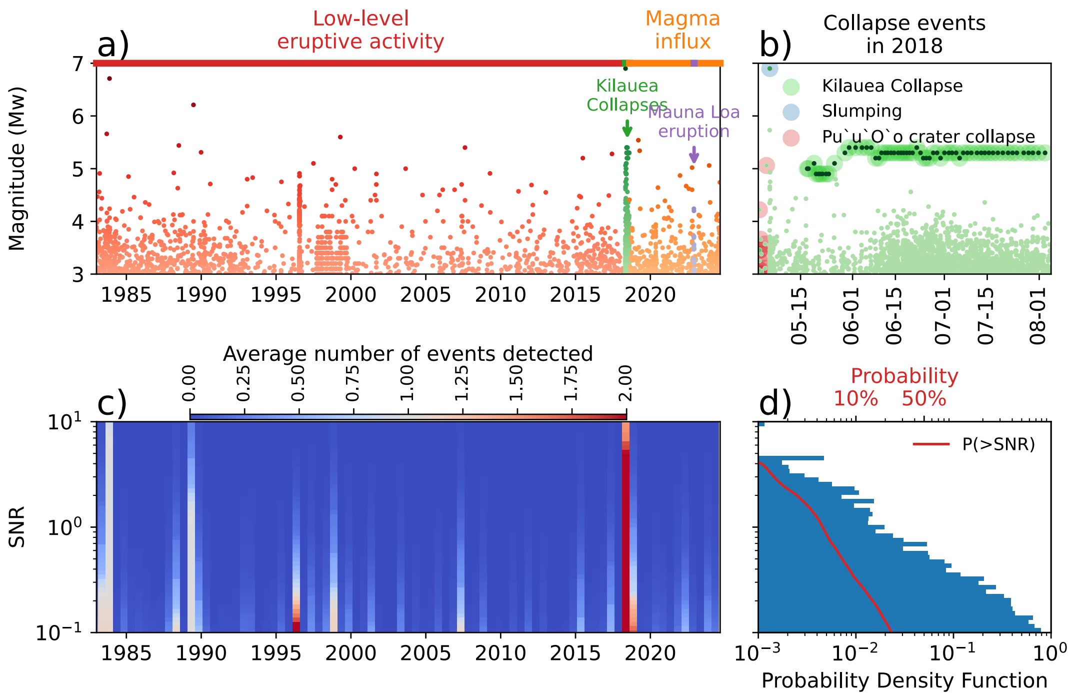

Figure 5. Volcanic sequence detection probability at 1 s for velocity model Cold100 at 50 km altitude. (a) Seismic events extracted from the Hawaiian Volcano Observatory catalog in Hawai'i. (b) Seismic events from May–August 2018 showing the largest tectonic earthquake (Slumping), Pu'u 'O'o crater collapses, and Kilauea collapse events. (c) Simulated average number of detected events on Venus v. Drop-off time and SNR across all drop-off locations. (d) Probability Density Function (blue histogram) and corresponding probability of observing a signal on Venus above a given SNR across the entire flight data set (P(> SNR), red).

driving processes behind the planet's volcanic activity, and provide additional constraints on its subsurface. Yet, previous studies have not explored the seismic potential of Venus' volcanoes. Indeed, scaling Earth volcanism to Venus is a challenging task. Some studies, such as Byrne and Krishnamoorthy (2022), have proposed a scaling of volcanic eruptions in terms of Volcanic Explosive Index (VEI), identifying the seismic contribution to the VEI requires several assumptions about volcanic source processes. Instead of introducing a large number of new scaling parameters to model volcanic seismicity, we opt to use seismic catalogs around well-instrumented Earth volcanoes as proxies for Venus volcanism.

There are several volcanoes on Venus with size and gravity signatures similar to hot-spot volcanoes on Hawai'i (Herrick & Hensley, 2023). In particular, Herrick and Hensley (2023) confirmed the recent deformation of a volcanic vent related to the Maat Mons volcano in Alta Regio on Venus with dimensions of the same order as the caldera collapse at Kilauea volcano, Hawai'i during the 2018 Kilauea eruption (Neal et al., 2019). The authors also speculated that some of the radar data near the event show a lava flow with, again, similar dimensions to the Kilauea Puna eruption in Hawai'i. Moreover, gentle slopes in Hawai'i shield volcanoes show similarities with Venus volcanoes such as Idunn Mons (D'Incecco et al., 2024). We therefore selected Mauna Loa and Kilauea calderas and their rift zones in Hawai'i as representative of typical seismicity in volcanic regions on Venus. This allows us to investigate variations of detectability not only in space but also in time for complex seismo-volcanic sequences, comprising explosive events, collapses, and deeper brittle failure events.

We extracted all seismic events above magnitude 3 in Hawai'i from the Hawaiian Volcano Observatory catalog (Figure 5a) since 1983—the onset of the Pu'u 'O'o eruption. Several driving processes can explain the variability in seismicity since 2012 (Figures 5a and 5b):

- (2012–2018) low-level eruptive activity from long-lived Pu'u 'O'o eruption with infrequent surficial activity and slow-moving, small lava fronts;
- (May 1–4 August2,018): Pu'u 'O'o crater floor collapse, causing a series of 62 $M_w > 5$ earthquakes at the summit;

- (4 May 2018) M_w 6.9 earthquake, below Kilauea's south flank, caused by slumping of the volcanic pile;
- (November 27—13 December 2022) First eruption at Mauna Loa following 38 years of quiescence;
- (2018–2024) Magma influx and small eruptions at Kilauea characterized by intermittent swarms of seismicity.

This data set is particularly interesting, as it includes a variety of source mechanisms such as collapse events and small lava flows, as has been observed on Venus. Here, we select the largest volcanic edifice on Venus, Maat Mons (8.7°N, 52.5°W), and assume that it produces the same seismicity as observed in Hawai'i. To provide meaningful detectability estimates, we simulate 15,000 flights with drop-off times every 6 months from 1983 to 2023 within 50° latitude and 50° longitude from the volcano.

Assuming that Maat Mons follows the same volcanic sequence as Hawai'i, the highest peak in number of events detected by the balloons, with SNR > 2 would occur in 2018 when slumping happens, producing a M_w 6.9 earthquake, together with repeating collapse events around M_w 5 (Figure 5c). However, the average number of events detected across all drop-off locations remains below 1 for most years even for low SNR (Figure 5c). Only swarms of seismic activity with magnitude above 4 can yield an average number of detections close to one (e.g., around 1996 and 2007). The probability of observing a signal with SNR > 1, integrated across all drop-off times, is around 5% for SNR $= 1$ and decreases to 2% for SNR $= 3$ (Figure 5d). For SNR > 1, detection probabilities of volcanic seismicity from a single volcano will therefore contribute to the overall detection probability $\mathbb{P}(Q \cup V)$ along with the tectonic event detection probability $\mathbb{P}(Q)$ (Figure 4c) as $\mathbb{P}(Q \cup V) = 1 - [1 - \mathbb{P}(Q)][1 - \mathbb{P}(V)] = 1 - [1 - 0.80][1 - 0.05] \approx 81\%$. While this suggests a minimal seismic contribution from volcanic seismicity to the detectability, we point out that volcanic events could occur around other volcanoes simultaneously (Byrne & Krishnamoorthy, 2022). Once again, these balloon detection probabilities can be extrapolated to airglow measurements and other periods using the results described in Section 3. At 100 s, we observe a significant drop in detection probabilities with maximum probabilities around 2% for SNR > 1 (SI 10).

5. Discussions and Limitations

For long-duration balloon missions, our results qualitatively agree with Garcia et al. (2024) in terms of detectability levels. Garcia et al. (2024) predicted a detection of at least one seismic event above M_w 5 (with a 66% confidence level) from a balloon and for a 3-month mission if 200 homogeneously distributed events occurred per year. Here, at 1 s, we reach the 66% confidence level for 3- to 3.5-month missions as well (Figure 4c). This good agreement is explained by our tectonic event catalog, producing about 150 events per year (Figure 1c), that is, on the same order as the minimum number of events predicted by Garcia et al. (2024). However, our seismic amplitude prediction model differs from Garcia et al. (2024), especially at 100 s (SI 3). This is mainly due to the use of Dirac sources in the current study and the limitations of the empirical model in Garcia et al. (2024). On one hand, Dirac source time functions do not capture the true magnitude-corner frequency relationship observed for earthquakes (Brune, 1970). On the other hand, the magnitude-period-amplitude relationship in Garcia et al. (2024) was initially designed for surface waves around 18−22 s period, and is not necessarily valid outside of this range.

Our airglow detectability model produces probabilities below 60% for both dayglow and nightglow, despite substantial temporal and spatial pixel binning, implying that seismic events are unlikely to be detected for low-seismicity scenarios. This is in disagreement with the much smaller number of M_w 5 seismic events required for a detection in Garcia et al. (2024) (about 6 for nightglow detection and 4 for dayglow detection) compared to the number of events included in our catalog. Our airglow amplitude model predicts significantly lower amplitudes than previous results (Kenda, 2018; Lognonné et al., 2016), despite relying on the same theory and approximations. Updated scaling factors between a unit ground vertical velocity and airglow photons emissions, show a decrease at 10 s of two orders of magnitude for the dayglow and three orders of magnitude for the nightglow compared to Garcia et al. (2024) (SI 12.5). Garcia et al. (2024) empirically extracted velocity-to-airglow scaling parameters from the data of a non-LTE simulation study (López-Valverde et al., 2011) and a model with plane-wave approximation (Sutin et al., 2018). Discrepancies likely originate from (a) the integration of realistic seismic waveforms along the VER column instead of simplistic sine-like waves, (b) the attenuation of acoustic waves up to the airglow layer altitude, and (c) the lower amplitudes predicted by our seismic amplitude model. We are also unable to reproduce the amplitude estimates from the analytical tests in Kenda (SI 12.4, 2018), which use sinusoidal inputs waveforms at the base of the airglow layer. Our simulations yield intensities smaller by a factor 3 in the dayglow and 100 in the nightglow. Interestingly, we are able to reproduce the nightglow amplitudes described in Sutin et al. (2018) with similar input waveforms as Kenda (2018) (SI 12.4). This suggests differences either in the numerical implementation of attenuation and amplification profiles or in the airglow equations in both works.

Another issue is the validation of the acoustic-to-airglow coupling model. For the 1.27 μm airglow, the formula of Lognonné et al. (2016) provides an approximation of the variation in concentration of excited O_2, and subsequent variations in 1.27 μm photon emission, following a wave perturbation. However, if only the vertical displacement component is considered, as in our simple approach, this perturbation has no net effect on intensity (SI 12.1). Therefore, we employed the model of Kenda (2018), which also accounts for the transport of background VER by the wave perturbation ($\mathbf{u} \cdot \nabla \mathrm{VER}$). Yet, only improved modeling could account for the precise dynamics of individual molecular species, as in Hickey et al. (2010), as well as high-altitude non-linear wave propagation processes (Inchin et al., 2020). For the 4.28 μm dayglow, we considered a simple emission model as described in Kenda (2018). For a more precise assessment of dayglow perturbation on Venus, more accurate models of the non-LTE emissions produced specifically by acoustic waves will be needed, as described in López-Valverde et al. (2011). Importantly, the validation of these advanced models would greatly benefit from the detection of seismically-induced airglow signals on Earth.

The detection probability at given drop-off locations would increase under more active seismicity scenarios, such as global venusquake rates on the order of terrestrial earthquakes (SI 11). However, such high rates are unlikely due to the absence of plate tectonics and global subduction networks (Ghail et al., 2024). Assuming all coronae to be active with subduction-like seismicity (as in Van Zelst et al., 2024b) likewise contradicts previous analyses of the diverse corona morphologies (Gülcher et al., 2025). On the other hand, lower seismicity levels, as proposed through Sabbeth et al. (2023)' wrinkle ridge model, result in small detection probabilities even at low SNR (SI 8). This highlights the need for further constraints on Venus seismicity through geodynamic simulations along with noise modeling (e.g., Gülcher et al., 2023). It should be noted that the wrinkle ridge seismicity estimates by Sabbeth et al. (2023) are likely conservative due to the use of a global map (Bilotti & Suppe, 1999), which does not resolve individual faults in detail. The tectonic scenarios considered here also exclude tesserae and other highly fractured terrains as seismically distinct from terrestrial intraplate settings.

Our probabilistic framework also assumes that the occurrence of tectonic venusquakes is described by a Poisson process. This is typically not the case when extracting events from global catalogs, like in Van Zelst et al. (2024b), primarily due to time-dependent foreshock and aftershock sequences. Declustering techniques are generally applied on a local scale to identify aftershocks or foreshocks (Gardner & Knopoff, 1974) with, more recently, machine learning providing more generic approaches to a variety of earthquake catalogs (Aden-Antoniów et al., 2022). However, applying such tools at a global scale is still challenging and will not correctly identify main shocks. Yet, as aftershocks typically decay quickly in magnitude with time, we can expect the number of lower-magnitude venusquakes $<M_w5$ to decrease, which will not significantly alter the detectability results presented here.

Seismicity is closely related to subsurface velocity structures. Our thermodynamical results indicate that in cases of high subsurface temperature profiles, large low-velocity zones are created, leading to smaller surface seismic motion and consequently reduced detection probability (Figures 4g–4i). Large uncertainties in the subsurface models therefore become a challenge if the goal is to provide robust detection probability estimates. In particular, seismic attenuation is a key parameter i.e. difficult to constrain, and our density mapping leads to an overly simplistic view of seismic quality factors. Future studies should revisit our mapping of AK135 quality factors to our Venus subsurface models by considering temperature-dependent profiles and by constraining several key parameters such as grain size and activation energy (e.g., Smrekar et al., 2019). Beyond tectonic seismicity, global volcanic seismicity could enhance detection probabilities, despite small final detection probabilities for a single volcano, if high seismic activity occurs at multiple volcanoes, which can be expected considering the abundance of volcanoes on Venus' surface (Bickel et al., 2025; Hahn & Byrne, 2023).

In addition to seismicity uncertainties, we made strong modeling assumptions to simplify the detection probability framework, which deserve further discussion to assess the robustness of our estimates: (a) A laterally homogeneous 1-D seismic model accurately represents Venus' interior, (b) Venus' surface has no topography, (c) Background atmospheric and airglow properties are not time dependent, and (d) Venus' deep atmosphere can be treated as an ideal gas, and (e) models of atmospheric attenuation are correct. All five assumptions will have an impact on the predicted body and surface-wave amplitudes recorded from a balloon or airglow imager. Lateral variations in seismic velocity lead to amplification and de-amplification of certain frequencies, as well as phase and surface wave mode conversions (Brissaud et al., 2020). In particular, high crust-mantle impedance contrasts can promote the trapping of energy close to the surface. Additionally, strong scattering occurs as surface waves travel across topography, especially when the dominant wavelength of the topography is of the same order as the dominant wavelength of the surface wave. Beyond seismic velocity models, background VER are considered homogeneous both in space and time which is not valid (Didion et al., 2018). VER amplitudes are expected to decrease away from the location of peak VER (typically near the subsolar or antisolar points), which would reduce the overall luminous intensity of the perturbation induced by acoustic waves, hence lowering the SNR. Additionally, spatial variations in density and sound velocity profiles can lead to changes in amplification above 100 km altitude. Atmospheric properties are also considered time independent, as sound velocity, pressure, and density variations are minimal throughout the year.

Furthermore, it is known that the CO_2 composing the deep atmosphere of Venus behaves more like a critical fluid than an ideal gas at its extreme temperature and pressure conditions. Averbuch and Petculescu (2025) showed that some variation in the sound velocity (about 5%) can be expected if applying a more general equation of state. Although this would not lead to significant changes in seismic-to-acoustic energy transmission, the authors also highlighted that at pressure and temperature closer to the critical point of CO_2, sound velocity could reach values close to zero, which would dramatically affect wave propagation within the first 10 km of Venus atmosphere. We should also mention that we did not consider direct infrasound from volcanic eruptions, which could be detected when a balloon is close to an active volcano. Beyond wave modeling assumptions, we extracted wind profiles on 15 June 2025, to simulate balloon trajectories. However, the wind patterns fluctuate between local day and night, and building more realistic balloon trajectory models with 3-D wind models can be important to better understand the trajectories and the associated noise levels. Note that we considered period-independent noise levels which is not valid in practice because environmental sources, wind noise and vortex shedding (Krishnamoorthy et al., 2020), balloon resonances (Garcia et al., 2022), balloon scattering (Godin, 2024) will affect recordings in various frequency bands. Our current model allows to explore other noise levels by changing the target SNRs. For example, doubling the noise level at 10 s is equivalent to doubling the requested SNR. At 10 s, the detection probabilities of 65% for a noise level of 0.01 Pa drops to about 50% for a noise level of 0.02 Pa (Figure 4e). In particular, near the eye of Venus' polar vortex, we can expect much less stable wind patterns that would deteriorate SNRs, meaning that detection probability could become dependent on balloon drop-off location (as opposed to SI 5).

6. Conclusions and Implications for Future Missions to Venus

Future joint balloon-airglow missions to Venus could provide an unprecedented level of detail about the subsurface. Our estimates for a 6-month mission suggest that detection probabilities for a at 10 s signal range from $\sim$75% for a single balloon, down to $\sim$65% for the detection of the same event by a balloon network, and below $\sim$60% for a detection by an airglow imager. Increasing the mission duration to 2 years, as suggested by Sutin et al. (2018), results in a doubling of the detection probability (SI 13). In parallel to air- and space-borne sensor developments, high-temperature seismometers could offer days-to month-long observations (Kremic et al., 2020). A 2-month seismometer mission, which is an optimistic scenario, would result in probabilities up to 75% near the coronae, similar to balloon borne detections (SI 14). We observe only minimal variations in the final detection probability over a 6-month mission when comparing the heterogeneous and homogeneous spatial distribution of venusquakes, despite the hourly detection levels varying up to 50% between the intraplate regions and the selected coronae (Figure 1a). Therefore, the drop-off location of a Venus balloon, provided it is outside of the polar caps, has no significant impact on the final detection probability at the mission end. When considering other subsurface models built from hotter thermal profiles (see Appendix A), we observe much lower detection probability, due to the absence of strong crustal waveguide (SI 7). Wrinkle Ridges seismicity shows 4 to 5 times lower probability of detection than tectonic seismicity. Our estimates indicate that each swarm of volcanically-induced seismicity with magnitude above 4 (triggered by edifice collapse, slumping, or eruptions) could contribute an increase of up to 1% in global seismicity for a single-balloon mission.

The ultimate goal of future missions is to identify body wave and/or surface wave arrivals to retrieve seismic velocities and/or seismic source properties. Accurate inversions of both source location and subsurface velocities requires the observation of the same event across at least three stations (Froment et al., 2025). Variation in distance and angular distribution between balloons of the network could affect inversions results and should be further investigated. Nevertheless, high-SNR signals are needed to measure body and surface waves arrival times or waveform shapes precisely. Assuming that signals with SNR = 2 would be enough to produce sufficiently constrained inversions of seismic velocities, our results show a median detection probability after 6 months of 45% at 1 s for a 3-balloon network (Figure 4f), which is too low to ensure mission success. Increasing the mission duration would steadily improve the detectability of high-SNR signals. In each frequency band, detectability follows a smooth second-order function of mission duration, allowing us to extrapolate that a 8- to 10-month mission would lead to the reference 66% confidence level of Garcia et al. (2024).

Note that our work did not account for any post-processing of balloon signals, which could provide alternative ways to increase the SNR. Equipping each balloon with several sensors along a tether (e.g., Brissaud et al., 2021) enables beamforming techniques to be applied to reduce incoherent noise. For example, airglow detection probabilities are increased by up to 60% when considering pixel and time binning, which removes incoherent noise, compared to the 5% without post-processing. However, the integration of volume emission rate perturbations along the line of sight both reduces the amplitude and affects the phase of airglow signals. In the context of seismic inversion, these effects could lead to imprecise measurements of surface wave dispersion at high frequency, increasing uncertainties in inverted seismic models (Kenda, 2018). Balloon pressure data are unaffected (Froment et al., 2025). Beyond subsurface velocity inversion, the event magnitude could be derived from the peak pressure amplitude and the source location, as it directly relates to peak ground velocity (Macpherson et al., 2023). However, determining the moment rate and *b*-value on Venus will be challenging from only a balloon network, due to the need to detect a large number of events. Indeed, the Martian moment rate, estimated using 55 events, still showed large uncertainties with values from 10^{15} to 10^{18} N m/year (Knapmeyer et al., 2023).

Our work further highlights the potential of balloon and joint balloon-airglow missions to Venus for the detection of seismic signals over 6 months to 1 year of observation. In particular, joint detections across balloon networks and an airglow imager would allow to capture seismic signals at both high and low frequencies, strengthening inversions of crustal and mantle properties. We identified several key assumptions that impact detection probabilities and require further investigation which can be ranked by importance: (a) Acoustic-to-airglow coupling model assumptions and validation, (b) Acoustic and airglow noise levels (detection probabilities estimates vary by 50% between SNR = 1 and SNR = 5), (c) Seismicity levels (current estimates can vary by orders of magnitudes depending on the moment rate of corona regions), (d) Mission duration (final detection probabilities follow a logarithmic trend with duration), and (e) Seismic velocity and attenuation models which impact the seismic-to-acoustic energy coupling (SI 7). The impact of these assumptions should be assessed in terms of both detectability versus SNR as well as posterior distributions of seismic velocities when performing inversions using balloon or airglow data. This would allow the community to refine mission and instrument design requirements.

Appendix A: Subsurface Velocity Models

As Venus' present-day interior thermal and lithological structure remains poorly constrained (e.g., Dumoulin et al., 2017; James et al., 2013), we consider several 1-D layered models of Venus' upper 300 km elastic structure that represent plausible lithological end-members. These profiles are generated by extrapolating Earth's shallow lithological layers to conditions envisioned for Venus' thermal and compositional state (Figure A1a,b). The thermal profiles correspond to the upper 300 km of two end-member geotherms, labeled M1 to M3 and corresponding to "hot" and "cold" scenarios, based on Dumoulin et al. (2017) and originally derived from Steinberger et al. (2010) and Armann and Tackley (2012) (Figure A1c). These profiles differ in mantle potential temperature (1600 K v. 1900 K) and adiabatic gradient (0.3 K/km v. 0.5 K/km). Figure A1d,e,f displays the resulting 1-D background seismic models used to compute the Green's functions in step (1).

To refine the uppermost lithospheric thermal structure, we employ a half-space cooling model (Turcotte & Schubert, 2002), commonly used in geodynamic modeling (e.g., Gülcher et al., 2020). This incorporates the relevant potential temperatures and adiabatic gradients along with different lithospheric ages: 10 and 25 Myr for the two "hot" profiles, and 100 Myr for the "cold" profile. These thermal profiles are combined with several 1-D internal layering profiles (Figure A1a). This layering is based on an underlying mineralogical model with depth-dependent mineral fractions that include ferric iron, computed using a two-step approach. First, we assume four distinct lithological end-members that could plausibly exist within Venus' crust-mantle system: granitoid crust,

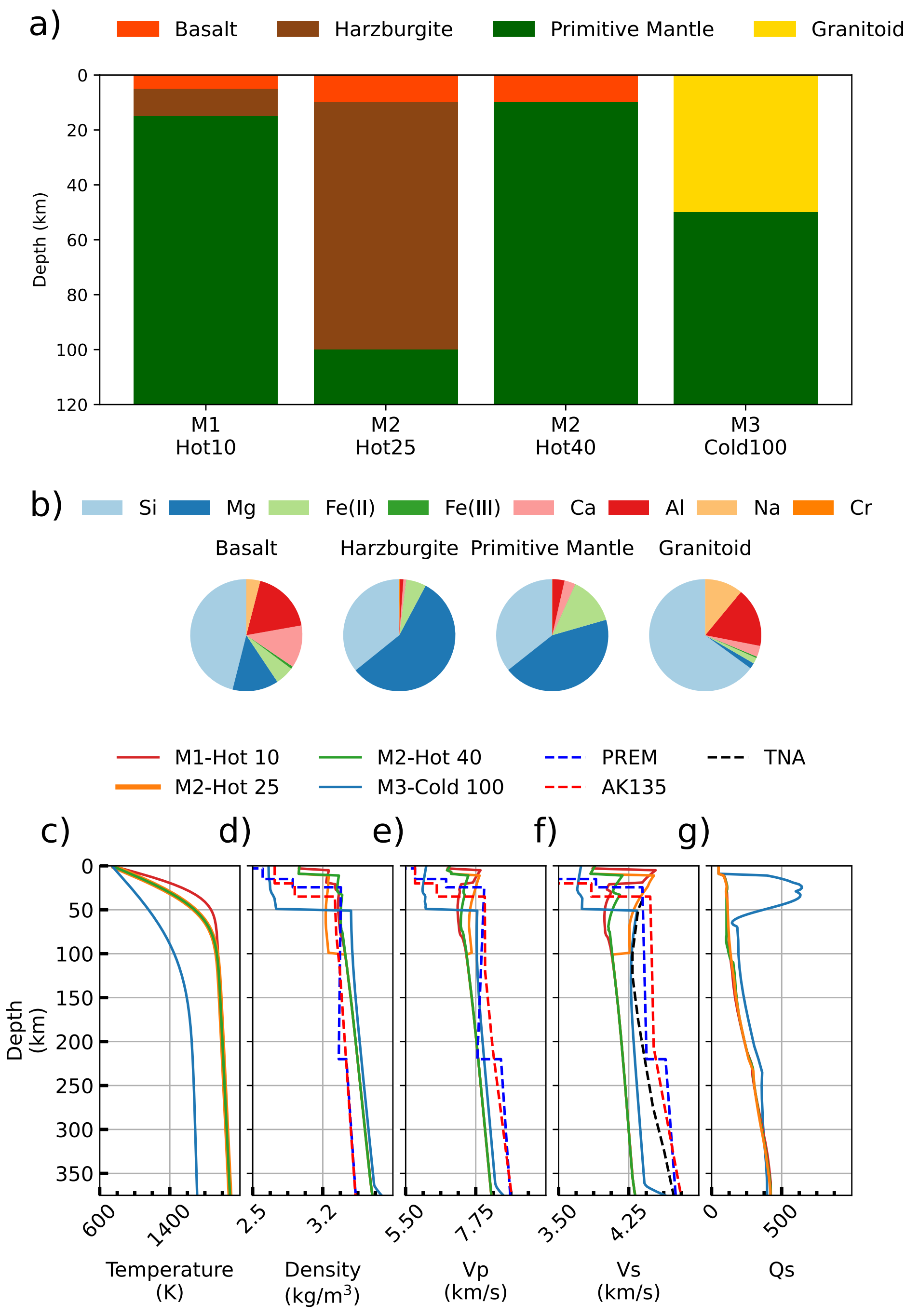

Figure A1. Construction of thermodynamically stable seismic velocity models. (a) 1-D layered thermochemical models M1 to M3, formulated by layered lithology and geotherms. We consider at most 3 layers representing crust, mantle lithosphere, and sub-lithosphere mantle. (b) Lithological end-member compositions in molar percentages. Basalt, harzburgite, are from Stixrude and Lithgow-Bertelloni (2024b), after Workman and Hart (2005) and Frost and McCammon (2008), and granitoid is modified from (Martin, 1994). Primitive mantle composition is modified from Dumoulin et al. (2017) (c, d, e, f) 1-D layered thermochemical models: M1 to M3, and their: (c) geotherm; (d) density; (e) P-wave velocity; (f) S-wave velocity; (g) S-wave quality factor. Elastic properties derived from Earth's global reference models, Preliminary Reference Earth Model (Dziewonski & Anderson, 1981) and ak135 (Kennett et al., 1995), are shown in (c, d, e, f). The regional shear-wave model TNA for western North America (Grand & Helmberger, 1984), shown for comparison.

basaltic crust, harzburgite-depleted mantle lithosphere, and the primitive mantle. The detailed chemical compositions of these end-members are shown in Figure A1b. We adopt basalt and harzburgite models from Stixrude and Lithgow-Bertelloni (2024a), a granitoid model representative of Archean-type continental crust from Martin (1994), and a primitive mantle composition estimated from solar nebula fractionation processes (Dumoulin et al., 2017; Morgan & Anders, 1980). We consider four thermomechanical structures, see Figure A1c,d,e,f.

Our hottest and thinnest lithosphere end-member, M1-Hot10, features a thin basaltic crust over a harzburgite-depleted mantle lithosphere and primitive mantle, combined with the hottest geotherm. This is representative of Venusian regions with lithospheric and crustal thinning, such as rift zones and some coronae (e.g., Sabbeth et al., 2023). The second structure, M2-Hot25, includes a slightly thicker basaltic crust (10 km) over a more substantial harzburgite-depleted lithosphere, underlain by the primitive mantle, combined with a hot but somewhat cooler lithosphere—representative of volcanic plains regions (e.g., James et al., 2013). The chemical boundary between the harzburgite lithosphere and the underlying primitive mantle may be blurred because of the effects of graded melting (e.g., Kelemen et al., 1992) and small-scale convection in the asthenosphere (e.g., Ballmer et al., 2007). To account for this, we adopt an additional end-member, M2-Hot40, derived from M2-Hot25, but where the harzburgite is thoroughly mixed with the primitive mantle. As an opposing end-member to basaltic crust models, we consider a thick granitoid crust over a cold lithosphere (M3-Cold100), as suggested for crustal plateau regions (e.g., Hans Wedepohl, 1995; Poldervaart, 1955).

The density and elastic properties of these models are calculated using temperature and pressure conditions derived from the chosen geotherms (Figure A1c). For each lithology and its pressure-temperature path, we use the thermodynamic software `HeFESTo` (Stixrude and Lithgow-Bertelloni, 2005, 2011, 2024a; Workman & Hart, 2005) to compute elastic properties. Unlike many previous models that only consider ferrous iron, our model incorporates ferric iron. `HeFESTo` determines phase equilibrium of a set of candidate mineral species by minimizing Gibbs free energy, and from that equilibrium computes the thermodynamic quantities of the assemblage at the specified conditions. We use `HeFESTo`'s default ambient-condition mantle species data set. In addition to velocity parameters, we include attenuation averaged from PREM at similar densities as our geological models (Figure A1g, SI 2). To account for larger scattering due to magma intrusion and unconsolidated material, we apply fixed attenuation parameters above 10 km depth, using low values observed near Kilauea, Hawai'i (Hansen et al., 2004).

Appendix B: Accounting for Balloon Trajectories

To account for the balloon motion, we compute trajectories $\mathbf{x}_{lat_0,lon_0,t_{\max}}$ up to a flight time $t_{\max}$ by considering a free-floating balloon at a constant altitude z_b, freely moving with Venus' horizontal winds, such that

$$\begin{aligned} \mathbf{x}_t^{\text{obs}} &= \mathbf{x}_{t-\Delta t}^{\text{obs}} + \mathbf{v}_{\text{wind}}\left(\mathbf{x}_{t-\Delta t}^{\text{obs}}\right)\Delta t \\ \mathbf{x}_0^{\text{obs}} &= \mathbf{x}_{lat_0,lon_0}, \end{aligned} \tag{B1}$$

where $\mathbf{x}_t^{\text{obs}}$ is the balloon location at time t, Δt (seconds) is the time step, $\mathbf{v}_{\text{wind}}\left(\mathbf{x}^{\text{obs}}\right)$ is the horizontal wind vector at location $\mathbf{x}^{\text{obs}}$, and $\mathbf{x}_{lat_0,lon_0}$ is the original balloon location. We can then compute the detection probability for a given balloon flight $\mathbb{P}(\text{SNR} > d, M_{\text{w,min}}, \mathbf{x}_{lat_0,lon_0}, t_{\max}, \sigma_n)$, up to a time $t_{\max}$ and from an origin location $\mathbf{x}_{lat_0,lon_0}$, by determining the probability of not detecting any event at each location along the balloon trajectory $\mathbf{t}$ such that,

$$\mathbb{P}(\text{SNR} > d, M_{\text{w,min}}, \mathbf{x}_{lat_0,lon_0}, t_{\max}, \sigma_n) = 1 - \prod_{i=0}^{N=\frac{t_{\max}}{\Delta t}} \left[1 - \mathbb{P}\left(\text{SNR} > d, M_{\text{w,min}}, x_{i\Delta t}^{\text{obs}}, \sigma_n, \Delta t\right)\right], \tag{B2}$$

where $\mathbb{P}\left(\text{SNR} > d, M_{\text{w,min}}, x_t^{\text{obs}}, \sigma_n, \Delta t\right)$ is given by Equation 2 and Δt (years) is the time step.

Appendix C: Incorporating a Balloon Network

Section 2.3 described the detection probability for a single balloon. However, deploying several balloons allows to (a) maximize the detection likelihood of venusquakes and (b) accurately retrieve event location and origin time.

To ensure the detection of the same event across the entire network above an SNR threshold, the signal amplitude at the balloon furthest from the source should be larger than said SNR threshold. Therefore, to determine the detection likelihood, we simply replace the station-to-venusquake distance r in Equation 4 by the maximum distance between a venusquake and all balloons, such that

$$\mathbb{P}(\mathrm{SNR} > d, \mathbf{x}^b|\mathrm{tec}) = \int_{M_\mathrm{w}=M_{\mathrm{w,min}}}^{M_{\mathrm{w,max}}} \int_{r=0}^{r_{\mathrm{Venus}}} \mathbb{P}(\mathrm{SNR} > d|M_\mathrm{w}, r) f_M^{\mathrm{tec}}(M_\mathrm{w}) f_{R,\mathrm{network}}^{\mathrm{tec}}(r, \mathbf{x}^b) dr dM_\mathrm{w}, \tag{C1}$$

where $(\mathbf{x}_n^b)_{n=1,N_{\mathrm{balloons}}}$ are the coordinates of each of the N_{balloons} balloons, and $f_{R,\mathrm{network}}^{\mathrm{tec}}(r, \mathbf{x}^b)$ is the PDF of an event occurring in the tectonic region at a distance r from the furthest sensor location:

$$f_{R,\mathrm{network}}^{\mathrm{tec}}(r, \mathbf{x}^b) = \mathbb{P}(R < r) = \frac{\partial}{\partial r} \frac{S_{\mathrm{network}}(r, \mathbf{x}^b) \cap S_{\mathrm{tec}}}{S_{\mathrm{tec}}}, \tag{C2}$$

$$S_{\mathrm{network}}(r) = \{P \in \mathrm{Venus} : \max(\mathrm{dist}(P, \mathbf{x}_1^b), \mathrm{dist}(P, \mathbf{x}_2^b), \ldots, \mathrm{dist}(P, \mathbf{x}_N^b)) \le r\}. \tag{C3}$$

Detecting the same event across the entire network is valuable for inversion, while the detection probability for any event by at least one balloon quantifies the benefit of a network versus a single sensor for improving venusquake sensitivity. This probability is obtained by replacing the maximum operator in Equation C3 by a minimum operator:

$$S_{\mathrm{network}}^{\mathrm{any\ event}}(r) = \{P \in \mathrm{Venus} : \min(\mathrm{dist}(P, \mathbf{x}_1^b), \mathrm{dist}(P, \mathbf{x}_2^b), \ldots, \mathrm{dist}(P, \mathbf{x}_N^b)) \le r\}. \tag{C4}$$

Appendix D: Incorporating Airglow Measurements

Airglow imagers onboard orbiters could provide a unique or complementary set of measurements together with a balloon network. Synthetic modeling shows that the perturbation of airglow emission by large earthquakes could be detectable on Earth (Inchin et al., 2020) and previous mission concepts have highlighted the potential for seismic-induced variations of the 1.27 μm nightglow and the 4.28 μm dayglow on Venus (Didion et al., 2018; Lognonné et al., 2016; Sutin et al., 2018). Garcia et al. (2024) provided airglow detectability estimates but made several assumptions about the underlying physics: (a) amplitudes are determined from an empirical magnitude-to-amplitude equation, and (b) the frequency dependence of the acoustic-to-airglow coupling is neglected despite having a strong influence on integrated airglow signals (Kenda, 2018, Section 4.3). Finally, Garcia et al. (2024) did not investigate the detectability of the same event using a hybrid balloon-airglow network.

Kenda (2018) summarize the equations required to approximate the acoustic-to-airglow coupling, assuming a purely vertical plane wave with velocity $v_z(z, t)$ and displacement $u_z(z, t)$ as initial atmospheric perturbation (Section 4.3 Kenda, 2018). Their derivation of the airglow intensity perturbation is described in SI 12. To also account for frequency-dependent attenuation, we integrate the absorption coefficient α along a vertical path such that

$$\mathcal{F}[v_z(M_\mathrm{w}, r, z, t)] = \mathcal{F}[v_z(M_\mathrm{w}, r, 0, \tilde{t}(t, z))] A(z, f), \tag{D1}$$

$$\tilde{t}(t, z) = t - \int_z dz/c(z), \tag{D2}$$

$$A(z, f) = \left[\frac{\rho(0)c(0)}{\rho(z)c(z)}\right]^{1/2} e^{-\int_z \alpha(f,z)dz}, \tag{D3}$$

where $\mathcal{F}$ is the Fourier transform, $v_z(M_\mathrm{w}, r, 0, t)$ (m/s) is the ground-velocity perturbation, for an event at a distance r and a magnitude M_w, as described in Section 2.2, and $\tilde{t}(t, z)$) is the propagation delay through the atmosphere. $A(z, f)$ is the combined amplification due to density decrease with altitude and attenuation. The airglow SNR, $\mathrm{SNR}_{\mathrm{airglow}}$, is then defined as the ratio of captured photons to shot noise $\sigma_{\mathrm{shot\ noise}}$ at a detector. The perturbation in captured photons can be computed as a disturbance over the total number of background photons, P, coming from

10.1029/2025EA004541

each layer and captured by a detector, where the disturbance is given by the VER perturbation produced by acoustic waves over the background VER:

$$\mathrm{SNR}_{\mathrm{airglow}}(M_{\mathrm{w}}, r) = \frac{\max_t [I(M_{\mathrm{w}}, r, t)]}{\int_{z_{\min}}^{z_{\max}} \mathrm{VER}(z)\, dz} \frac{P}{\sigma_{\text{shot noise}}} \tag{D4}$$

$$I(M_{\mathrm{w}}, r, t) = \int_{z_{\min}}^{z_{\max}} \delta \mathrm{VER}(M_{\mathrm{w}}, r, z, t)\, dz. \tag{D5}$$

The shot noise is assumed to be the dominant source of noise and is given by $\sigma_{\text{shot noise}} \approx \sqrt{P}$. For a specific orbiting camera configuration, Kenda (2018) estimate $P^{1.27} \approx 2e^4$, $P^{4.28} \approx 3.5e^5$. The perturbation δVER is given for 1.27 and 4.28 μm layers as

$$\delta \mathrm{VER}^{1.27}(M_{\mathrm{w}}, r, z, t) = \mathcal{F}^{-1}\left[-\frac{\tau}{1 + i\omega\tau}\mathcal{F}\left[\mathrm{VER}(z)\frac{\partial}{\partial z}v_z(M_{\mathrm{w}}, r, z, t)\right]\right] \tag{D6}$$

$$\delta \mathrm{VER}^{4.28}(M_{\mathrm{w}}, r, z, t) = \alpha(\gamma - 1)\mathrm{T}(z)\mathrm{VER}(z)\left[\frac{\partial}{\partial z}u_z(M_{\mathrm{w}}, r, z, t) + \frac{u_z(M_{\mathrm{w}}, r, z, t)}{\rho_0(z)}\frac{\partial}{\partial z}\rho_0(z)\right] \tag{D7}$$

$$-u_z(M_{\mathrm{w}}, r, z, t)\frac{\partial}{\partial z}\mathrm{VER}(z), \tag{D8}$$

where $\mathcal{F}^{-1}$ is the inverse Fourier transforms, $\omega = 2\pi f$ is the pulsation, $\tau = 4460$ s (Kenda, 2018, Section 4.3) is the radiative lifetime of excited oxygen in the nightglow, $\alpha = 1\%$ is the sensitivity of dayglow emission rate to a temperature perturbation in the 4.28 μm layer, and $u(z, t)$ (m) is the displacement perturbation defined from the time integration of Equation D1.

To incorporate airglow data within the probabilistic framework, the surface area defined by source-station distances in Equation 7 is rescaled to account for both the higher propagation altitude to the airglow layer, as well as the conversion from acoustic wave to airglow. Scaled source-receiver distances $R = r + \tilde{r}$ for airglow can be found by solving for $\tilde{r}$, that is, the horizontal distance parameter for which pressure SNR at the balloon altitude and at a distance $r + \tilde{r}$ is equal to airglow SNR at a distance r:

$$\frac{\mathrm{TL}(M_{\mathrm{w}}, R = r + \tilde{r})}{\sigma_n} = \beta\, \mathrm{SNR}_{\mathrm{airglow}}(M_{\mathrm{w}}, r), \tag{D9}$$

where β is the pixel and time binning factor. Instead of performing intricate modeling of individual airglow waveforms, we pre-compute scaling factors $S_a(M_{\mathrm{w}}, r)$ between a unit ground velocity and the resulting integrated VER perturbation, $\max_t [I(M_{\mathrm{w}}, r, t)] / \int_{z_{\min}}^{z_{\max}} \mathrm{VER}(z)\, dz$, along each VER column, such that $\mathrm{SNR}_{\mathrm{airglow}}(M_{\mathrm{w}}, r) = S_a(M_{\mathrm{w}}, r)\sqrt{P}(\times 1 \text{ m/s})$. To capture the frequency dependence of airglow coupling, the scaling factor $S_a(M_{\mathrm{w}}, r)$ is calculated at 1, 0.1 and 0.01 Hz, taking its median value for a range of source distances and depths. An advantage of airglow imagers is the large FOV, with a 60° radius centered around the satellite location (115×10^6 km^2) for an orbit at 45 000 km altitude (Didion et al., 2018). Each pixel in the airglow imager's FOV acts as an independent sensor providing timeseries of airglow perturbations Binning $\beta \times \beta$ pixels or *beta* time steps increases the SNR by a factor β.

Finally, to account for the large FOV, we modify the surface area from airglow location $\mathbf{x}^{\mathrm{airglow}}$ out to distance r:

$$\mathcal{S}^{\mathrm{airglow}}(r, \mathbf{x}^{\mathrm{airglow}}) = \mathcal{S}\left(r - r_0^{\mathrm{airglow}}, \mathbf{x}^{\mathrm{airglow}}\right) \cup \left[\mathcal{S}_{\mathrm{FOV}}^{\mathrm{airglow}}(\mathbf{x}^{\mathrm{airglow}}) \cap \mathcal{S}_{\mathrm{AEA}}^{\mathrm{airglow}}\right], \tag{D10}$$

where $\mathcal{S}_{\mathrm{FOV}}^{\mathrm{airglow}}(\mathbf{x}^{\mathrm{airglow}})$ is a surface cap of radius r_0^{airglow} centered around the imager location $\mathbf{x}$ and $\mathcal{S}_{\mathrm{AEA}}^{\mathrm{airglow}}$ is the Airglow Emission Area (AEA) for each layer. For the 1.27 μm emission, the AEA is centered on the equatorial point at 10:00 local time, covering an angular radius of ~60 degrees around this point (115×10^6 km^2). For the

4.28 μm emission, the AEA is centered on the equatorial point at 12:00 local time, covering an angular radius of $\sim$70 degrees (151×10^6 km^2) (Garcia et al., 2024).

Current mission concepts assume a high-altitude orbit at $R = 45\,000$ km (Didion et al., 2018), requiring 35 hr to complete an orbit. Such spacecraft can therefore probe both dayglow and airglow within a 2-day span.

Conflict of Interest

The authors declare no conflicts of interest relevant to this study.

Availability Statement

The detection probability framework and data are already available on a Figshare repository (Brissaud et al., 2026) corresponding to the first version of the codes and data available at https://github.com/QuentinBrissaud/Venus_Detectability. The airglow amplitude prediction software is available on a Figshare repository (Brissaud & Froment, 2026) corresponding to the first version of the codes and data available at https://github.com/QuentinBrissaud/airglow_model. Both repositories will be cleaned and documented upon paper acceptation. Tectonic setting shape files and moment rates are available at Van Zelst et al. (2024a). Wrinkle ridges spatial distribution and moment rates are available at Sabbeth (2023). The thermodynamic software HeFESTo (Stixrude & Lithgow-Bertelloni, 2005) is available at https://github.com/stixrude/HeFESToRepository.

Acknowledgments

This work received support from the Airborne Inversion of Rayleigh wave (AIR) project, funded by the Research Council of Norway basic research program FRIPRO, Contract 335903, as well as NORSAR institute funding. We thank the Norwegian national e-infrastructure for computational science, Sigma2, for high-performance computational resources through the University of Oslo Project number NN8104K. A. G. acknowledges funding from the Center for Space and Habitability at the University of Bern as well as NCCR PlanetS supported by the Swiss National Science Foundation under Grant 51NF40_205,606. J. M. J. thanks the JPL Strategic Research and Technology Development Program, "Venus Science Into the Next Decade" and the W. E. Keck Institute for Space Studies. We are grateful to Carolina Lithgow-Bertelloni and Lars Stixrude for helpful discussions regarding HeFESTo. The authors thank Wenbo Wu and Yasuhiro Nishikawa for their insightful reviews.

References

Aden-Antoniów, F., Frank, W. B., & Seydoux, L. (2022). An adaptable random forest model for the declustering of earthquake catalogs. *Journal of Geophysical Research: Solid Earth*, *127*(2), e2021JB023,254. https://doi.org/10.1029/2021jb023254

Aki, K. (1972). Scaling law of earthquake source time-function. *Geophysical Journal International*, *31*(1–3), 3–25. https://doi.org/10.1111/j.1365-246x.1972.tb02356.x

Armann, M., & Tackley, P. J. (2012). Simulating the thermochemical magmatic and tectonic evolution of Venus's mantle and lithosphere: Two-dimensional models. *Journal of Geophysical Research*, *117*(E12), E12003. https://doi.org/10.1029/2012JE004231

Averbuch, G., Houston, R., & Petculescu, A. (2023). Seismo-acoustic coupling in the deep atmosphere of Venus. *Journal of the Acoustical Society of America*, *153*(3), 1802–1810. https://doi.org/10.1121/10.0017428

Averbuch, G., & Petculescu, A. (2025). Calculating the acoustic and internal gravity wave dispersion relations in Venus's supercritical lower atmosphere. *Journal of the Acoustical Society of America*, *157*(4), 3180–3191. https://doi.org/10.1121/10.0036505

Ballmer, M. D., van Hunen, J., Ito, G., Tackley, P. J., & Bianco, T. A. (2007). Non-hotspot volcano chains originating from small-scale sub-lithospheric convection. *Geophysical Research Letters*, *34*(23), https://doi.org/10.1029/2007GL031636

Bethell, E. M., Ernst, R. E., & Samson, C. (2019). Geology of the alpha regio (V-32) quadrangle, Venus. *Journal of Maps*, *15*(2), 474–486. https://doi.org/10.1080/17445647.2019.1614489

Bickel, V. T., Johnson, C. L., & Russell, M. B. (2025). Revisiting volcanism on Venus with deep learning, in. In *Proceedings of the 56th lunar and planetary science conference*. Lunar and Planetary Institute, The Woodlands, Texas, USA, abstract 1387.

Bilotti, F., & Suppe, J. (1999). The global distribution of wrinkle ridges on Venus. *Icarus*, *139*(1), 137–157. https://doi.org/10.1006/icar.1999.6092

Brissaud, Q., Bowden, D. C., & Tsai, V. C. (2020). Extension of the basin Rayleigh-wave amplification theory to include basin-edge effects. *Bulletin of the Seismological Society of America*, *110*(3), 1305–1322. https://doi.org/10.1785/0120190161

Brissaud, Q., & Froment, M. (2026). Airglow response to seismic rayleigh waves on Venus (version 1.0) [software]. *figshare*. https://doi.org/10.6084/m9.figshare.32328057

Brissaud, Q., Kong, C., Froment, M., Wilding, J. D., Gülcher, A. J. P., Jackson, J. M., et al. (2026). Datasets and codes for "aerial and space-borne seismology on venus: Viability and design implications for future missions" (version 1.0) [dataset]. *figshare*. https://doi.org/10.6084/m9.figshare.32326602

Brissaud, Q., Krishnamoorthy, S., Jackson, J. M., Bowman, D. C., Komjathy, A., Cutts, J. A., et al. (2021). The first detection of an earthquake from a balloon using its acoustic signature. *Geophysical Research Letters*, *48*(12), e2021GL093013. https://doi.org/10.1029/2021gl093013

Brune, J. N. (1970). Tectonic stress and the spectra of seismic shear waves from earthquakes. *Journal of Geophysical Research*, *75*(26), 4997–5009. https://doi.org/10.1029/jb075i026p04997

Byrne, P. K., & Krishnamoorthy, S. (2022). Estimates on the frequency of volcanic eruptions on Venus. *Journal of Geophysical Research: Planets*, *127*(1), e2021JE007040. https://doi.org/10.1029/2021je007040

Cascioli, G., Gülcher, A. J. P., Mazarico, E., & Smrekar, S. E. (2025). A spectrum of tectonic processes at coronae on Venus revealed by gravity and topography, science advances. *11*(20), eadt5932. https://doi.org/10.1126/sciadv.adt5932

Cornell, C. A. (1968). Engineering seismic risk analysis. *Bulletin of the Seismological Society of America*, *58*(5), 1583–1606. https://doi.org/10.1785/bssa0580051583

Davaille, A., Smrekar, S. E., & Tomlinson, S. (2017). Experimental and observational evidence for plume-induced subduction on Venus. *Nature Geoscience*, *10*(5), 349–355. https://doi.org/10.1038/ngeo2928

Didion, A., Komjathy, A., Sutin, B., Nakazono, B., Karp, A., Wallace, M., et al. (2018). *Remote sensing of Venusian seismic activity with a small spacecraft, the VAMOS mission concept, in 2018 IEEE aerospace conference*, (pp. 1–14). IEEE. https://doi.org/10.1109/AERO.2018.8396447

D'Incecco, P., Filiberto, J., Garvin, J., Arney, G., Getty, S., Ghail, R., et al. (2024). Mount Etna as a terrestrial laboratory to investigate recent volcanic activity on Venus by future missions: A comparison with idunn mons, Venus. *Icarus*, *411*, 115,959,. https://doi.org/10.1016/j.icarus.2024.115959

Dombard, A. J., Johnson, C. L., Richards, M. A., & Solomon, S. C. (2007). A magmatic loading model for coronae on Venus. *Journal of Geophysical ResearchEducational Planning*, *112*(4), 1–13. https://doi.org/10.1029/2006JE002731
Dumoulin, C., Tobie, G., Verhoeven, O., Rosenblatt, P., & Rambaux, N. (2017). Tidal constraints on the interior of Venus. *Journal of Geophysical Research: Planets*, *122*(6), 1338–1352. https://doi.org/10.1002/2016je005249
Dziewonski, A. M., & Anderson, D. L. (1981). Preliminary reference Earth model. *Physics of the Earth and Planetary Interiors*, *25*(4), 297–356. https://doi.org/10.1016/0031-9201(81)90046-7
Froment, M., Brissaud, Q., Näsholm, S. P., & Schweitzer, J. (2025). Balloon seismology enables subsurface inversion without ground stations. *Communications Earth and Environment*, *6*(1), 949. https://doi.org/10.1038/s43247-025-02917-7
Frost, D. J., & McCammon, C. A. (2008). The redox state of earth's mantle. *Annual Review of Earth and Planetary Sciences*, *36*(1), 389–420. https://doi.org/10.1146/annurev.earth.36.031207.124322
Garcia, R. F., Klotz, A., Hertzog, A., Martin, R., Gérier, S., Kassarian, E., et al. (2022). Infrasound from large earthquakes recorded on a network of balloons in the stratosphere. *Geophysical Research Letters*, *49*(15), e2022GL098,844. https://doi.org/10.1029/2022GL098844
Garcia, R. F., Van Zelst, I., Kawamura, T., Näsholm, S. P., Horleston, A., Klaasen, S., et al. (2024). Seismic wave detectability on Venus using ground deformation sensors, infrasound sensors on balloons and airglow imagers. *Earth and Space Science*, *11*(11), e2024EA003670. https://doi.org/10.1029/2024EA003670
Gardner, J., & Knopoff, L. (1974). Is the sequence of earthquakes in southern California, with aftershocks removed, poissonian? *Bulletin of the Seismological Society of America*, *64*(5), 1363–1367. https://doi.org/10.1785/BSSA0640051363
Gerier, S., Garcia, R. F., Martin, R., & Hertzog, A. (2024). Forward modeling of quake's infrasound recorded in the stratosphere on board balloon platforms, Earth. *Planets and Space*, *76*(1), 87. https://doi.org/10.1186/s40623-024-02030-7
Ghail, R. C., Smrekar, S. E., Widemann, T., Byrne, P. K., Gülcher, A. J., O'Rourke, J. G., et al. (2024). Volcanic and tectonic constraints on the evolution of Venus. *Space Science Reviews*, *220*(4), 36. https://doi.org/10.1007/s11214-024-01065-2
Godin, O. A. (2024). Fidelity of infrasound measurements with balloon-borne sensors. *Journal of the Acoustical Society of America*, *156*(6), 3909–3920. https://doi.org/10.1121/10.0034562
Grand, S. P., & Helmberger, D. V. (1984). Upper mantle shear structure of North America. *Geophysical Journal International*, *76*(2), 399–438. https://doi.org/10.1111/j.1365-246x.1984.tb05053.x
Grindrod, P. M., & Hoogenboom, T. (2006). Venus: The Corona conundrum. *Astronomy and Geophysics*, *47*(3), 3.16–3.21. https://doi.org/10.1111/j.1468-4004.2006.47316.x
Gülcher, A. J. P., Gerya, T. V., Montési, L. G. J., & Munch, J. (2020). Corona structures driven by plume–lithosphere interactions and evidence for ongoing plume activity on Venus. *Nature Geoscience*, *13*(8), 547–554. https://doi.org/10.1038/s41561-020-0606-1
Gülcher, A. J. P., Sabbeth, L., Stofan, E., & Smrekar, S. E. (2025). Coronae on Venus: An updated global database and insights into morphology, spatial distribution, geological setting, and lithospheric properties. *Journal of Geophysical Research: Planets*, *130*(5), e2024JE008749. https://doi.org/10.1029/2024JE008749
Gülcher, A. J. P., Yu, T.-Y., & Gerya, T. V. (2023). Tectono-magmatic evolution of asymmetric coronae on Venus: Topographic classification and 3D thermo-mechanical modeling. *Journal of Geophysical Research: Planets*, *128*(11), e2023JE007978. https://doi.org/10.1029/2023JE007978
Hahn, R. M., & Byrne, P. K. (2023). A morphological and spatial analysis of volcanoes on Venus. *Journal of Geophysical Research: Planets*, *128*(4), e2023JE007753. https://doi.org/10.1029/2023JE007753
Hansen, S., Thurber, C., Mandernach, M., Haslinger, F., & Doran, C. (2004). Seismic velocity and attenuation structure of the east rift zone and south flank of Kilauea volcano, Hawaii. *Bulletin of the Seismological Society of America*, *94*(4), 1430–1440. https://doi.org/10.1785/012003154
Hans Wedepohl, K. (1995). The composition of the Continental crust. *Geochimica et Cosmochimica Acta*, *59*(7), 1217–1232. https://doi.org/10.1016/0016-7037(95)00038-2
Heimann, S., Vasyura-Bathke, H., Sudhaus, H., Isken, M. P., Kriegerowski, M., Steinberg, A., & Dahm, T. (2019). A python framework for efficient use of pre-computed Green's functions in seismological and other physical forward and inverse source problems. *Solid Earth*, *10*(6), 1921–1935. https://doi.org/10.5194/se-10-1921-2019
Herrick, R. R., & Hensley, S. (2023). Surface changes observed on a Venusian volcano during the Magellan mission. *Science*, *379*(6638), 1205–1208. https://doi.org/10.1126/science.abm7735
Hickey, M., Schubert, G., & Walterscheid, R. (2010). Atmospheric airglow fluctuations due to a tsunami-driven gravity wave disturbance. *Journal of Geophysical Research*, *115*(A6). https://doi.org/10.1029/2009JA014977
Hoogenboom, T., & Houseman, G. A. (2006). Rayleigh-taylor instability as a mechanism for Corona formation on Venus. *Icarus*, *180*(2), 292–307. https://doi.org/10.1016/j.icarus.2005.11.001
Inchin, P., Snively, J., Williamson, A., Melgar, D., Aguilar Guerrero, J., & Zettergren, M. (2020). Mesopause airglow disturbances driven by nonlinear infrasonic acoustic waves generated by large earthquakes. *Journal of Geophysical Research: Space Physics*, *125*(6), e2019JA027,628,. https://doi.org/10.1029/2019JA027628
James, P. B., Zuber, M. T., & Phillips, R. J. (2013). Crustal thickness and support of topography on Venus. *Journal of Geophysical Research: Planets*, *118*(4), 859–875. https://doi.org/10.1029/2012je004237
Kelemen, P. B., Dick, H. J. B., & Quick, J. E. (1992). Formation of harzburgite by pervasive melt/rock reaction in the upper mantle. *Nature*, *358*(6388), 635–641. https://doi.org/10.1038/358635a0
Kenda, B. (2018). Planetary applications of atmospheric seismology: Signals from the Martian turbulent atmosphere and observation perspectives in Venus' ionosphere, Master's thesis, Institut de Physique du Globe de Paris.
Kennett, B. L. N., Engdahl, E. R., & Buland, R. (1995). Constraints on seismic velocities in the Earth from traveltimes. *Geophysical Journal International*, *122*(1), 108–124. https://doi.org/10.1111/j.1365-246X.1995.tb03540.x
Knapmeyer, M., Stähler, S., Plesa, A.-C., Ceylan, S., Charalambous, C., Clinton, J., et al. (2023). The global seismic moment rate of Mars after event S1222a. *Geophysical Research Letters*, *50*(7), e2022GL102296. https://doi.org/10.1029/2022GL102296
Kremic, T., Ghail, R., Gilmore, M., Hunter, G., Kiefer, W., Limaye, S., et al. (2020). Long-duration Venus lander for seismic and atmospheric science. *Planetary and Space Science*, *190*, 104961. https://doi.org/10.1016/j.pss.2020.104961
Krishnamoorthy, S., Bowman, D. C., Komjathy, A., Pauken, M. T., & Cutts, J. A. (2020). Origin and mitigation of wind noise on balloon-borne infrasound microbarometers. *Journal of the Acoustical Society of America*, *148*(4), 2361–2370. https://doi.org/10.1121/10.0002356
Krishnamoorthy, S., Lai, V. H., Komjathy, A., Pauken, M. T., Cutts, J. A., Garcia, R. F., et al. (2019). Aerial seismology using balloon-based barometers. *IEEE Transactions on Geoscience and Remote Sensing*, *57*(12), 10191–10201. https://doi.org/10.1109/TGRS.2019.2931831
Lebonnois, S., Hourdin, F., Eymet, V., Crespin, A., Fournier, R., & Forget, F. (2010). Superrotation of venus' atmosphere analyzed with a full general circulation model. *Journal of Geophysical Research*, *115*(E6). https://doi.org/10.1029/2009je003458

Lebonnois, S., Millour, E., Martinez, A., Pierron, T., Bierjon, A., Forget, F., et al. (2022). *The Venus climate database, in abstract B4.1-0013-22*. Greece. https://doi.org/10.5194/epsc2021-234

Lebonnois, S., Sugimoto, N., & Gilli, G. (2016). Wave analysis in the atmosphere of Venus below 100-km altitude, simulated by the LMD Venus GCM. *Icarus*, *278*, 38–51. https://doi.org/10.1016/j.icarus.2016.06.004

Lognonné, P., Banerdt, W. B., Clinton, J., Garcia, R. F., Giardini, D., Knapmeyer-Endrun, B., et al. (2023). Mars seismology. *Annual Review of Earth and Planetary Sciences*, *51*(1), 643–670. https://doi.org/10.1146/annurev-earth-031621-073318

Lognonné, P., Karakostas, F., Rolland, L., & Nishikawa, Y. (2016). Modeling of atmospheric-coupled rayleigh waves on planets with atmosphere: From Earth observation to Mars and Venus perspectives. *Journal of the Acoustical Society of America*, *140*(2), 1447–1468. https://doi.org/10.1121/1.4960788

López-Valverde, M., López-Puertas, M., Funke, B., Gilli, G., Garcia-Comas, M., Drossart, P., et al. (2011). Modeling the atmospheric limb emission of co2 at 4.3 μm in the terrestrial planets. *Planetary and Space Science*, *59*(10), 988–998. https://doi.org/10.1016/j.pss.2010.02.001

Macpherson, K. A., Fee, D., Colwell, J. R., & Witsil, A. J. (2023). Using local infrasound to estimate seismic velocity and earthquake magnitudes. *Bulletin of the Seismological Society of America*, *113*(4), 1434–1456. https://doi.org/10.1785/0120220237

Maia, J., Plesa, A.-C., Van Zelst, I., Brissaud, Q., De Toffoli, B., Garcia, R., et al. (2024). Constraining the seismogenic thickness of Venus, in europlanet science congress 2024. *A peer-reviewed journal paper version of this work has been accepted for publication in Journal of Geophysical Research: Planets, expected to become available in July 2025*, *17*, EPSC2024–915.

Martin, H. (1994). The Archean grey gneisses and the genesis of Continental crust. *Developments in Precambrian Geology*, *11*, 205–259. https://doi.org/10.1016/S0166-2635(08)70224-X

Martinez, A., Lebonnois, S., Millour, E., Pierron, T., Moisan, E., Gilli, G., & Lefèvre, F. (2023). Exploring the variability of the Venusian thermosphere with the IPSL Venus GCM. *Icarus*, *389*, 115272. https://doi.org/10.1016/j.icarus.2022.115272

Morgan, J. W., & Anders, E. (1980). Chemical composition of Earth, Venus, and Mercury. *Proceedings of the National Academy of Sciences*, *77*(12), 6973–6977. https://doi.org/10.1073/pnas.77.12.6973

Neal, C. A., Brantley, S., Antolik, L., Babb, J., Burgess, M., Calles, K., et al. (2019). The 2018 rift eruption and summit collapse of Kīlauea volcano. *Science*, *363*(6425), 367–374. https://doi.org/10.1126/science.aav7046

Phillipson, G., Sobradelo, R., & Gottsmann, J. (2013). Global volcanic unrest in the 21st century: An analysis of the first decade. *Journal of Volcanology and Geothermal Research*, *264*, 183–196. https://doi.org/10.1016/j.jvolgeores.2013.08.004

Piskorz, D., Elkins-Tanton, L. T., & Smrekar, S. E. (2014). Coronae formation on Venus via extension and lithospheric instability. *Journal of Geophysical Research: Planets*, *119*(12), 2568–2582. https://doi.org/10.1002/2014JE004636

Poldervaart, A. (1955). Chemistry of the earth's crust (pp. 119–144).

Price, M., & Suppe, J. (1995). Constraints on the resurfacing history of venus from the hypsometry and distribution of volcanism, tectonism, and impact craters, Earth. *The Moon and the Planets*, *71*(1–2), 99–145. https://doi.org/10.1007/bf00612873

Price, M. H., Watson, G., Suppe, J., & Brankman, C. (1996). Dating volcanism and rifting on venus using impact crater densities. *Journal of Geophysical Research*, *101*(E2), 4657–4671. https://doi.org/10.1029/95je03017

Sabbeth, L. (2023). Estimated seismicity of venusian wrinkle ridges based on fault scaling relationships. *Zenodo*. https://doi.org/10.5281/zenodo.8011379

Sabbeth, L., Smrekar, S., & Stock, J. (2023). Estimated seismicity of Venusian wrinkle ridges based on fault scaling relationships. *Earth and Planetary Science Letters*, *619*, 118,308. https://doi.org/10.1016/j.epsl.2023.118308

Sandwell, D. T., & Schubert, G. (1992). Evidence for retrograde lithospheric subduction on Venus. *Science*, *257*(5071), 766–770. https://doi.org/10.1126/science.257.5071.766

Schools, J., & Smrekar, S. (2024). Formation of coronae topography and fractures via plume buoyancy and melting. *Earth and Planetary Science Letters*, *633*(118643), 118643. https://doi.org/10.1016/j.epsl.2024.118643

Smrekar, S. E., Lognonné, P., Spohn, T., Banerdt, W. B., Breuer, D., Christensen, U., et al. (2019). Pre-mission insights on the interior of Mars. *Space Science Reviews*, *215*(1), 3. https://doi.org/10.1007/s11214-018-0563-9

Steinberger, B., Werner, S. C., & Torsvik, T. H. (2010). Deep versus shallow origin of gravity anomalies, topography and volcanism on Earth, Venus and Mars. *Icarus*, *207*(2), 564–577. https://doi.org/10.1016/j.icarus.2009.12.025

Stixrude, L., & Lithgow-Bertelloni, C. (2005). Thermodynamics of mantle minerals – I. Physical properties. *Geophysical Journal International*, *162*(2), 610–632. https://doi.org/10.1111/j.1365-246X.2005.02642.x

Stixrude, L., & Lithgow-Bertelloni, C. (2011). Thermodynamics of mantle minerals – II. Phase equilibria. *Geophysical Journal International*, *184*(3), 1180–1213. https://doi.org/10.1111/j.1365-246X.2010.04890.x

Stixrude, L., & Lithgow-Bertelloni, C. (2024a). Thermodynamics of mantle minerals–iii: The role of iron. *Geophysical Journal International*, *237*(3), 1699–1733. https://doi.org/10.1093/gji/ggae126

Stixrude, L., & Lithgow-Bertelloni, C. (2024b). Thermodynanics of mantle minerals – III. The role of iron. *Geophysical Journal International*, *237*(3), 1699–1733. https://doi.org/10.1093/gji/ggae126

Sulcanese, D., Mitri, G., & Mastrogiuseppe, M. (2024). Evidence of ongoing volcanic activity on Venus revealed by Magellan radar. *Nature Astronomy*, *8*(8), 1–10. https://doi.org/10.1038/s41550-024-02272-1

Sutin, B. M., Cutts, J., Didion, A. M., Drilleau, M., Grawe, M., Helbert, J., et al. (2018). VAMOS: A SmallSat mission concept for remote sensing of Venusian seismic activity from orbit, in space telescopes and instrumentation 2018: Optical, infrared, and millimeter wave, Vol. *10698*, (pp. 1651–1670). https://doi.org/10.1117/12.2309439

Turcotte, D. L., & Schubert, G. (2002). In *Geodynamics* (2 ed.). Cambridge University Press. https://doi.org/10.1017/CBO9780511807442

Van Zelst, I., Maia, J., Plesa, A.-C., Ghail, R., & Spühler, M. (2024a). Data and scripts - Estimates on the possible annual seismicity of Venus. *Zenodo*. https://doi.org/10.5281/zenodo.12166635

Van Zelst, I., Maia, J. S., Plesa, A.-C., Ghail, R., & Spühler, M. (2024b). Estimates on the possible annual seismicity of Venus. *Journal of Geophysical Research: Planets*, *129*(7), e2023JE008,048. https://doi.org/10.1029/2023JE008048

Wang, R., Heimann, S., Zhang, Y., Wang, H., & Dahm, T. (2017). Complete synthetic seismograms based on a spherical self-gravitating Earth model with an atmosphere–ocean–mantle–core structure. *Geophysical Journal International*, *210*(3), 1739–1764. https://doi.org/10.1093/gji/ggx259

Widemann, T., Smrekar, S. E., Garvin, J. B., Straume-Lindner, A. G., Ocampo, A. C., Schulte, M. D., et al. (2023). Venus evolution through time: Key science questions, selected mission concepts and future investigations. *Space Science Reviews*, *219*(7), 56. https://doi.org/10.1007/s11214-023-00992-w

Workman, R. K., & Hart, S. R. (2005). Major and trace element composition of the depleted MORB mantle (DMM). *Earth and Planetary Science Letters*, *231*(1), 53–72. https://doi.org/10.1016/j.epsl.2004.12.005